Research Proposal to Jefferson Lab PAC 29

Deeply Virtual Compton Scattering with CLAS at 6 GeV

H. Avakian, S. Boyarinov, V.D. Burkert[1], L. Elouadrhiri[1], R. Niyazov, S. Stepanyan[1,2], Yu. Sharabian, E. Smith, M. Vanderhaeghen
Jefferson Lab, Newport News, VA 23606, USA

J. Ball, P. Bertin, A. Camsonne, R. De Masi, C. Ferdi, M. Garçon[1], F.-X. Girod, M. Guidal, H.-S. Jo, M. Mazouz, M. Mac Cormick, B. Michel, C. Muñoz Camacho, S. Niccolai, F. Sabatié, E. Voutier
LPC (Clermont) / LPSC (Grenoble) / IPNO (Orsay) / SPhN (Saclay)
CEA/DSM/DAPNIA & CNRS/IN2P3, France

I. Bedlinskiy, S. Kuleshov, O. Pogorelko
Institute of Theoretical and Experimental Physics, Moscow, 117259, Russia

N. Dashyan, K. Egiyan
Yerevan Physics Institute, Yerevan, Armenia 375036

K. Joo, N. Markov, M. Ungaro, B. Zhao
University of Connecticut, Storrs, CT 06269, USA

V. Kubarovsky, P. Stoler
Rensselaer Polytechnic Institute, Troy, NY 12181, USA

M.J. Amarian, G. Dodge, C.E. Hyde-Wright, H.G. Juengst, S.E. Kuhn, A. Radyushkin, L. Weinstein
Old Dominion University, Norfolk, VA 23529, USA

D.S. Carman
Ohio University, Athens, OH 45701, USA

C. Smith
University of Virginia, Charlottesville, VA 22901, USA

[1] Co-spokesperson
[2] Contact person

Abstract

We propose to study Deep Virtual Compton Scattering (DVCS) using the CEBAF 6 GeV polarized electron beam and the CLAS detector at Jefferson Lab. The main focus of the experiment will be measurement of the beam spin asymmetry in the reaction $\vec{e}p \rightarrow ep\gamma$. This asymmetry is directly proportional to the imaginary part of the DVCS amplitude and gives access to a combination of the Generalized Parton Distributions H, E, and $\tilde{H}$. The Q^2, x_B and t dependence of the DVCS amplitude will be studied in a wide range of kinematics. In addition, helicity-dependent cross section differences will be measured. In some kinematics, we will be able to determine the unpolarized DVCS cross section by subtracting the Bethe-Heitler contribution. 60 days of beam time were approved by PAC20 for this experiment with priority A. 36 days were used successfully in a first run in spring 2005. Taking into account the integrated luminosity during this first run, 34 days of beam time are now requested to complete the experiment.

Contents

1 Foreword **4**

2 Introduction **5**

3 Theory and motivation **6**
3.1 Phenomenology of the GPDs 6
3.2 Deeply Virtual Compton Scattering 9

4 Experimental situation **12**
4.1 Evidence from JLab with CLAS 12
4.2 JLab proposals 12
4.2.1 Hall B - E99-105 13
4.2.2 Hall A - E00-110 and E03-106 14
4.2.3 Hall-B - E05-114 14
4.3 Experiments at HERA 14
4.3.1 HERMES 14
4.3.2 H1 and ZEUS experiments 15
4.4 CERN experiment 15

5 Experiment E01-113 **17**
5.1 CLAS configuration during the Spring 2005 run 17
5.2 Superconducting solenoid magnet 19
5.3 $PbWO_4$ crystal calorimeter 19
5.3.1 Performance of the calorimeter 22
5.3.2 Event reconstruction with CLAS 25
5.4 Measurement of radiation damage in IC 25
5.5 Status of the data analysis 26

6 Event identification and reconstruction **32**

7 Count rates and statistical errors **35**
7.1 Systematic errors 36
7.2 Projected results and comparison to models 38

8 Summary and beam time request **42**

1 Foreword

This is an update on proposal E01-113, which was recommended by PAC20 in July 2001 with priority "A". Although the authors of the initial proposal requested running the experiment in a single beam period, and were technically ready to do so, the 2005 accelerator and experimental schedule could accommodate only 36 out of the total allocated time of 60 days. The DVCS collaboration built, commissioned and installed two new devices in CLAS, a superconducting solenoid magnet and a 424-channel $PbWO_4$ crystal calorimeter. Both devices were critical for this experiment and both showed excellent performance during the run.

Although a significant amount of data was collected, we are short of achieving the goals of the original proposal E01-113 in terms of mapping out Q^2, x_B and t dependences of the DVCS beam spin asymmetry. We now seek new approval (under jeopardy) for 34 days, necessary to achieve the goals of proposal E01-113.

The text of this proposal follows the initial proposal E01-113, with the following additions or updates:

- Update of the author list
- Update and complement the GPD phenomenology section (Sec. 3.1),
- Update the experimental situation (Sec. 4), reflecting the fact that experiments E99-105 and E00-110 are now completed, and that HERMES is about to install a recoil detector for a new campaign of DVCS measurements; in this context, the delay in completing experiment E01-113 in Hall B puts us in direct competition, as far as the calendar is concerned, with HERMES.
- Incorporate several small corrections or additions (these do not alter the arguments and the main points developed in proposal E01-113),
- Sec. 5 is specific to this proposal update to the CEBAF PAC29. It gives the performances of the equipment built, tested, inserted in CLAS and used successfully in spring 2005. We are now in a phase of detector calibration and data reduction. We have clear evidence that the new Inner Calorimeter (IC) and magnetic shielding performed successfully at the designed luminosity and that $ep \rightarrow ep\gamma$ events will be identified unambiguously.
- Without being exhaustive, update and complement the bibliography.

2 Introduction

Much of the internal structure of the nucleon has been revealed during the past three decades through the inclusive scattering of high-energy leptons on nucleons in the Bjorken -or "Deeply Inelastic Scattering" (DIS)- regime. Simple theoretical interpretations of the experimental results and quantitative conclusions can be reached in the framework of the parton model and QCD when one sums over all possible hadronic final states. For instance, *unpolarized* DIS led to the discovery of the quark and gluon substructure of the nucleon, with the quarks carrying about half of the nucleon's momentum. Furthermore, *polarized* DIS revealed that only about 25% of the spin of the nucleon is carried by the quark intrinsic spin. However, very little is known about quark-quark correlations, the transverse quark momentum distribution, and contributions of correlated quark-antiquark pairs (mesons) to the nucleon wave function.

The recently developed formalism of "Generalized Parton Distributions" (GPDs) [1, 2] showed that such information can be obtained in hard exclusive leptoproduction experiments. The GPDs contain information on the interference between different quark configurations, on the quark transverse momentum distribution, as well as their angular momentum distribution. GPDs provide a unifying picture for an entire set of fundamental quantities of hadronic structure, such as: the vector and axial vector nucleon form factors, the polarized and unpolarized parton distributions, and the spin components of the nucleon due to orbital excitations.

Deeply Virtual Compton Scattering (DVCS) is one of the key reactions to determine the GPDs experimentally, and it is the simplest process that can be described in terms of GPDs. We propose a measurement of DVCS in Hall B at Jefferson Lab with a 6 GeV longitudinally polarized electron beam, with a CLAS configuration optimized for running at higher luminosity, 2×10^{34} cm^{-2}s^{-1}, and with a larger acceptance for photon detection.

The first experimental observation of exclusive DVCS was obtained from our published analysis of CLAS data with a 4.25 GeV polarized electron beam in a limited kinematical regime around $Q^2 = 1.25$ GeV^2 and $x_B = 0.19$ [3]. The new measurements will map out the DVCS amplitude in the range of Q^2 from 1 to 4 GeV^2, and x_B from 0.15 to 0.55. The main goal will be a study of the x_B and t dependence of the beam spin asymmetry. These measurements are essential for the study of GPDs.

The CLAS detector with the proposed new configuration and a 6 GeV longitudinally polarized electron beam form a unique facility to perform such measurements with a single experimental setup in a wide range of kinematics.

3 Theory and motivation

3.1 Phenomenology of the GPDs

We briefly review in this section the formalism of the Generalized Parton Distributions. Ji [1] and Radyushkin [2] (see also Ref. [4]) have shown that the Deeply Virtual Compton scattering (DVCS) amplitude in the forward direction can be factorized in leading-order pQCD into a hard-scattering part (exactly calculable in pQCD) and a non-perturbative nucleon structure part, as illustrated in Fig. 1a. In these so-called "handbag" diagrams, the lower blob represents the soft structure of the nucleon, and can be described in terms of four structure functions, known as the GPDs.

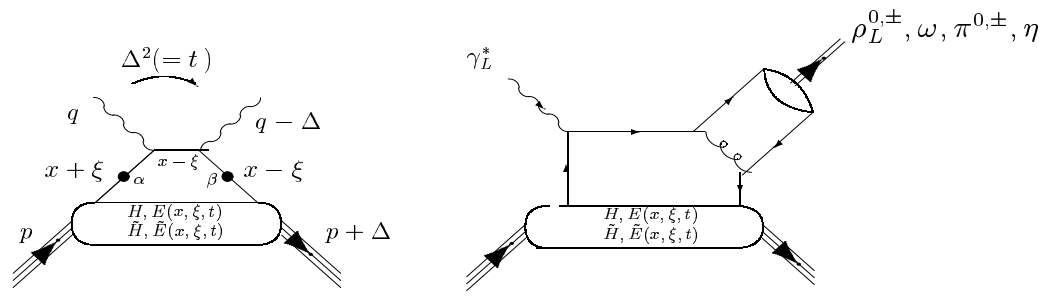

Figure 1: "Handbag" diagrams for (a) DVCS (left) and (b) meson production (right).

There are 4 independent GPDs: $H, \tilde{H}, E$, and $\tilde{E}$; they depend upon three kinematic variables: x, ξ, and t. x characterizes the momentum fraction of the struck quark in the quark loop and, as such, is not directly accessible experimentally except in the measurement of the beam spin asymmetry. ξ is the longitudinal momentum fraction of the transfer Δ, with $\xi = x_B/(2-x_B)$ in the Bjorken limit. $t = \Delta^2$ is the standard momentum transfer between the virtual and real photons.

H and E are so-called spin-independent, and $\tilde{H}$ and $\tilde{E}$ are spin-dependent functions. More precisely, the light-cone matrix element of the bilocal quark operator that enters in these hard-electroproduction reactions (represented by the lower blobs in Fig. 1) is at leading twist in Q^2 given by:

$$\begin{aligned}
&\frac{P^+}{2\pi}\int dy^- e^{ixP^+y^-}\langle p'|\bar{\Psi}_\beta(-\frac{y}{2})\Psi_\alpha(\frac{y}{2})|p\rangle\Big|_{y^+=\vec{y}_\perp=0} \\
&= \frac{1}{4}\Big\{(\gamma^-)_{\alpha\beta}\left[H^q(x,\xi,t)\ \bar{N}(p')\gamma^+N(p)\ +\ E^q(x,\xi,t)\ \bar{N}(p')i\sigma^{+\kappa}\frac{\Delta_\kappa}{2M_N}N(p)\right] \\
&\quad +(\gamma_5\gamma^-)_{\alpha\beta}\left[\tilde{H}^q(x,\xi,t)\ \bar{N}(p')\gamma^+\gamma_5N(p)\ +\ \tilde{E}^q(x,\xi,t)\ \bar{N}(p')\gamma_5\frac{\Delta^+}{2M_N}N(p)\right]\Big\} \quad (1)
\end{aligned}$$

with $P = (p+p')/2$ and q a quark flavor index. This formula explicitly shows the

vector (axial) nature of the H, E ($\tilde{H}$, $\tilde{E}$) GPDs associated or not associated with the γ_5 matrix.

The H and $\tilde{H}$ are generalizations of the parton distributions measured in deep inelastic scattering. In the forward direction (defined by $\Delta = 0$), H reduces to the quark distribution $q(x)$, and $\tilde{H}$ to the quark-helicity distribution $\Delta q(x)$ measured in deep inelastic scattering. Furthermore, at finite momentum transfer, there are model-independent sum rules that relate the first moments of these GPDs to the standard hadronic form factors:

$$\begin{aligned} \int_{-1}^{1} H^q(x,\xi,t)dx &= F_1^q(t), \\ \int_{-1}^{1} E^q(x,\xi,t)dx &= F_2^q(t), \\ \int_{-1}^{1} \tilde{H}^q(x,\xi,t)dx &= G_A^q(t), \\ \int_{-1}^{1} \tilde{E}^q(x,\xi,t)dx &= G_P^q(t), \quad \forall\xi \end{aligned} \tag{2}$$

Also, Ji [1] has shown that the second moment of these GPDs gives access to the contribution of the sum of the quark spin and the quark orbital angular momentum to the nucleon spin.

$$\forall\xi, \quad \lim_{t\to 0} \frac{1}{2} \sum_q \int_{-1}^{1} x \left[H^q(x,\xi,t) + E^q(x,\xi,t) \right] dx \;=\; J_{quarks} \tag{3}$$

A measurement of this sum rule would determine the contribution of the quark orbital angular momentum to the nucleon spin. However, we point out that this is not within the goals of the proposed experiment.

The GPDs reflect the structure of the nucleon independently of the reaction that probes the nucleon. They can also be accessed through the hard exclusive electroproduction of mesons, $\pi^{0,\pm}$, $\rho^{0,\pm}$, ω, ϕ,..., (see Fig. 1b) for which a QCD factorization proof was given [5]. It also showed that leading-order pQCD predicts that the vector meson channels ($\rho_L^{0,\pm}$, ω_L, ϕ_L) are sensitive only to the unpolarized GPDs (H and E), whereas the pseudoscalar channels ($\pi^{0,\pm}, \eta, ...$) are sensitive only to the polarized GPDs ($\tilde{H}$ and $\tilde{E}$). In contrast to meson electroproduction, DVCS depends on *both* the polarized and unpolarized GPDs.

Models of GPDs were obtained by direct calculations in the bag model [6], chiral soliton model [7], light-cone formalism [8], and also through a phenomenological construction [9, 10] based on the relation of GPDs to the usual parton densities.

Figure 2 shows the x and ξ dependence of $H(x,\xi,t=0)$ as an example of such a construction. The ξ dependence shows the changing character of the quark correlations from pure quark and antiquark distributions at $\xi = 0$, to strongly correlated $q\bar{q}$ pairs at large values of ξ.

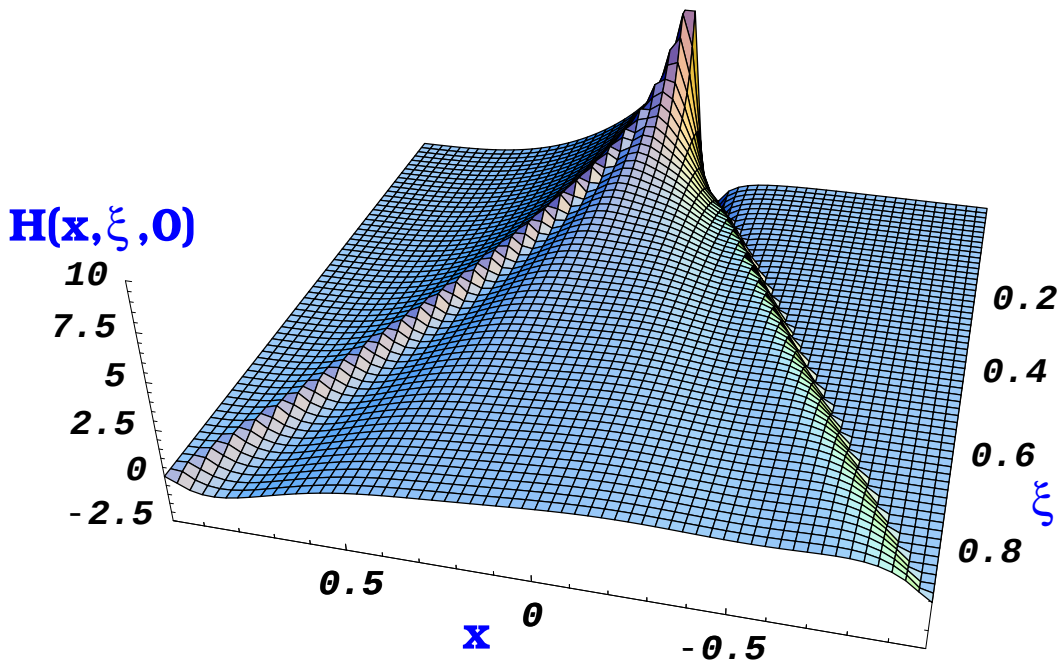

Figure 2: $H(x, \xi, 0)$ in the model of Ref. [10].

The shape and magnitude of the GPDs also depends on the momentum transfer t. This opens up another dimension in the study of GPDs. The t dependence is particularly sensitive to the transverse distribution of the quarks. This could lead to a simultaneous measurement of the longitudinal momentum fraction and transverse position of partons [11], which may develop into a "femto-photography" of the proton [12].

Since PAC20 and our original proposal, the interest in GPDs has continued growing. This is exemplified by many reviews [13, 14, 15, 16, 17, 18]. A short introduction to the subject is presented in Ref. [19]. Briefly and without proper reference to all the work done, we list hereafter the main theoretical developments:

- The GPDs may be viewed as part of a still wider class of parton distributions (six-dimensional Wigner distributions) which allow one to make a link with Transverse Momentum Distributions (TMD) accessible in semi-inclusive scattering.

- The "3D" picture of the nucleon emerging from the correlation between transverse position and longitudinal momentum is that high-x quarks are mostly in the nucleon core while low-x partons are at the periphery. This is substantiated by "Regge inspired" parametrizations of GPDs, by constraints from elastic form factors, and also by the first lattice calculations on the subject. Moments of GPDs can be calculated on the lattice (still with a pion mass that is too large), and a sufficient number of moments, together with some intuitive inputs, allows one to reconstruct GPDs. However, the determination of the real x-t correlations still awaits experimental developments such as the one proposed here.

- Many models point to a significant orbital angular momentum of the quarks in the nucleon, at least for individual flavors (one view is that both u and d quarks have large orbital angular momentum, but that the sum would be small).

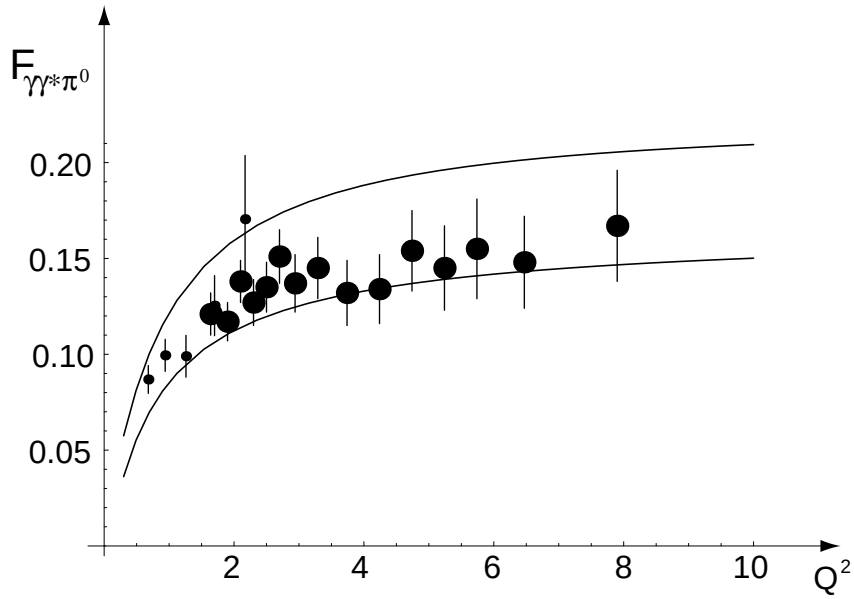

Figure 3: Experimental data on $Q^2 F_{\gamma^*\gamma\pi^0}$ from [20] with pQCD predictions using an asymptotic shape for the pion distribution amplitude (lower curve) and the Chernyak-Zhitnitsky model (upper curve). The calculations include higher order corrections.

- Although at the heart of the introduction of the concept of GPDs, their off-diagonal character (x-ξ correlations) has not been the subject of many recent theoretical investigations. In this respect, JLab is in a unique position to access significantly higher values of ξ, or to probe the off-diagonal character of the GPDs.

- Finally, new parametrizations of GPDs are being proposed, which could be used in the future for a global fit to the relevant data.

3.2 Deeply Virtual Compton Scattering

DVCS is the most promising channel for studying GPDs at lower energies and Q^2. The dominance of the handbag diagram and the behavior of the reduced forward cross section as $1/Q^4$ (scaling regime) is expected to be reached at lower Q^2 than in the case of deep exclusive meson production. This is supported by measurements of the $\gamma^*\gamma\pi^0$ form-factor in e^-e^+ collisions. In leading-order pQCD, the DVCS process and the production of π^0 by two photons, where one of the photons is highly virtual, are described by the same kind of handbag diagram. Figure 3 shows measurements of $F_{\gamma^*\gamma\pi^0}$ from CLEO [20]. The curves correspond to leading order pQCD calculations [21] with next to leading order corrections. As is evident from the figure, $F_{\gamma^*\gamma\pi^0}$ starts to scale as $1/Q^2$ already at $Q^2 \sim 3$ GeV^2. The higher order corrections describe the data well for $Q^2 > 1$ GeV^2. This result strongly suggests that GPDs can be accessed through the study of DVCS at moderate Q^2.

The proposed experiment measures DVCS via the interference with the Bethe-Heitler (BH) process, Figure 4. The measured cross section of the reaction $ep \rightarrow ep\gamma$ is given by the sum of the DVCS and BH amplitudes, up to a phase space factor:

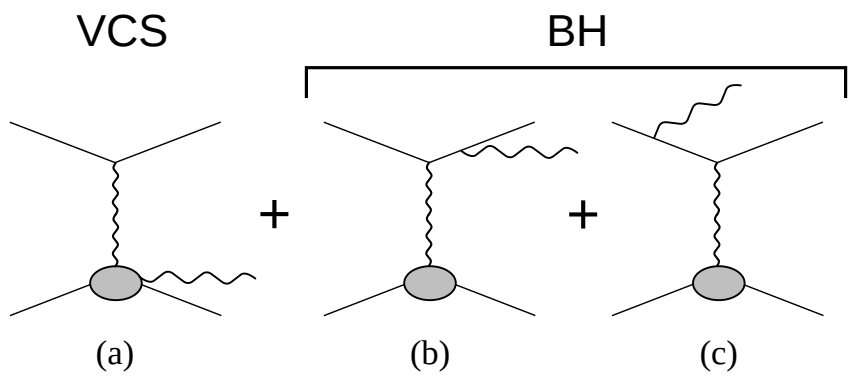

Figure 4: Feynman diagrams for VCS and Bethe-Heitler processes contributing to the amplitude of $ep \to ep\gamma$ scattering.

$$\frac{d^5\sigma}{dQ^2 dx_B dt d\phi} \propto |\mathcal{T}^{VCS} + \mathcal{T}^{BH}|^2 . \tag{4}$$

At beam energies accessible at Jefferson Lab, the BH contribution in the cross section is predicted to be several times larger than the DVCS contribution in most regions of phase space [10] (see Fig. 5).

The large BH process may be turned into an advantage by using a longitudinally polarized electron beam: one can measure the helicity-dependent interference terms that are proportional to the imaginary part of the DVCS amplitude. In this case the pure BH contribution is subtracted out in the cross section difference. The systematic errors then only apply to this difference. Expanding the BH amplitude in powers of $1/Q$, but keeping the complete helicity structure for the $\gamma^* p \to \gamma p$ process [23], the helicity-dependent cross section difference is given by:

$$\frac{d^5\sigma^+}{dQ^2 dx_B dt d\phi} - \frac{d^5\sigma^-}{dQ^2 dx_B dt d\phi} \propto \mathrm{Im}(\mathcal{T}^{DVCS}) \times \mathcal{T}^{BH}$$
$$\propto \frac{1}{Q}\left[-\sqrt{\frac{1+\epsilon}{\epsilon}} \cdot \mathrm{Im}\tilde{M}^{1,1} \cdot \sin\phi + \mathrm{Im}\tilde{M}^{0,1} \cdot \sin 2\phi\right] + \mathcal{O}\left(\frac{1}{Q^2}\right) \tag{5}$$

where "+" and "-" denote positive and negative beam helicities. $\mathcal{T}^{DVCS}$ and $\mathcal{T}^{BH}$ are the amplitudes of the DVCS and BH processes, ϵ is the usual virtual photon polarization parameter, ϕ is the azimuthal angle between electron and hadron planes, and $\tilde{M}^{1,1}$ and $\tilde{M}^{0,1}$ are helicity amplitudes for transverse and longitudinal virtual photons, averaged over the proton helicity. In leading order, only $\tilde{M}^{1,1}$ contributes, and, therefore, the dominant $\sin\phi$ dependence should be observed. Note that, in addition to the interference term in Eq. (5), the cross section difference also contains

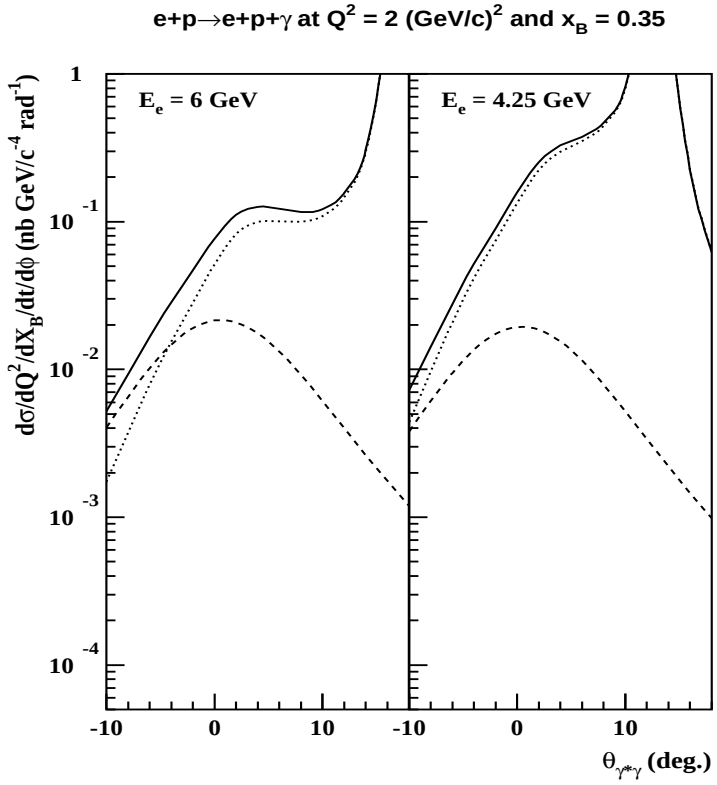

Figure 5: Cross section of $ep \rightarrow ep\gamma$ as a function of the angle between the virtual and real photons at beam energies of 4.25 (right) and 6 GeV (left), for $Q^2 = 2$ GeV^2 and $x_B = 0.35$. The positive values of $\theta_{\gamma\gamma^*}$ correspond to $\phi = 0$, and the negative to $\phi = 180°$. The dashed line is the contribution of DVCS, the dotted line represents the Bethe-Heitler part, and the solid line is the total sum (Eq. (4)). The cross sections are calculated according to Ref. [22].

pure DVCS $\sin\phi$ terms, of the order $|\tilde{M}^{1,1}\tilde{M}^{0,1}|/Q^2$; these are twist-3 terms, with a small effect on the observable in our kinematics, as illustrated in Sec. 7.2.

The beam spin asymmetry is simply obtained from the ratio of the expressions (5) and (4):

$$BSA \equiv \frac{\sigma^+ - \sigma^-}{\sigma^+ + \sigma^-} = \frac{\sigma^+ - \sigma^-}{2\sigma} \tag{6}$$

The denominator is dominated by a ϕ independent BH term, but contains also, to lower order in $1/Q$, ϕ dependent terms with contributions both from pure BH and from the BH-DVCS interference. The latter may be expressed as a function of the real parts $\mathrm{Re}\tilde{M}^{\lambda,1}$ [23].

The predicted beam spin asymmetries are sizeable; they are illustrated in Figs. 6. Different parameterizations of the GPD's affect the magnitude of this asymmetry, while higher-order corrections such as twist-3 contributions have little effect on this observable [24].

An important aspect of the measurements of cross section differences for different helicities is that they probe GPDs at specific values of x, assuming the dominance of the handbag diagram: in this case, $\mathrm{Im}\tilde{M}^{1,1}$ is given by a sum of GPDs at $x = \pm\xi$. The same is true for the numerator of the beam spin asymmetry. This allows one

to obtain more direct information on the x dependence of the GPDs. In contrast, in cross section measurements, GPDs appear in convolution integrals over x, through $\mathrm{Re}\tilde{M}^{1,1}$.

Note that the DVCS process may also be calculated from a non-perturbative Regge model, where the real photon is associated to a transition from a transverse ρ meson [25].

4 Experimental situation

4.1 Evidence from JLab with CLAS

The DVCS/BH interference has recently been measured for the first time using CLAS. The data were collected as a by-product during the 1999 e1 run with a 4.25 GeV polarized electron beam. At energies above 4 GeV, the CLAS acceptance covers a wide range of kinematics in the deep inelastic scattering domain (W $\geq$ 2 GeV and $Q^2 \geq 1$ GeV^2). The open acceptance of CLAS and the use of a single electron trigger ensures event recording for all possible final states. For the DVCS analysis, the reaction $\vec{e}p \rightarrow epX$ was studied and the number of single photon final states was extracted by fitting the missing mass (M_X^2) distributions. When compared to other reports (see Sec. 4.3), this may be considered as the first truly exclusive DVCS signal.

The beam spin asymmetry is calculated as:

$$BSA = \frac{1}{P_e}\frac{\left(N_\gamma^+ - N_\gamma^-\right)}{\left(N_\gamma^+ + N_\gamma^-\right)} \tag{7}$$

Here P_e is the beam polarization, $N_\gamma^{+(-)}$ is the extracted number of $ep \rightarrow ep\gamma$ events at positive (negative) beam helicity.

The resulting ϕ-dependence is shown in Fig. 6. A fit to the function

$$A(\phi) = \alpha \sin\phi + \beta \sin 2\phi \tag{8}$$

yields $\alpha = 0.217 \pm 0.031$ and $\beta = 0.027 \pm 0.022$. If the handbag diagram dominates, in the Bjorken regime, β should vanish and only the contribution from transverse photons should remain, described by parameter α.

4.2 JLab proposals

At the Jefferson Laboratory, three other experiments were performed for the study of exclusive reactions, with the initial aim to test whether the hard scattering regime may be reached at $Q^2 < 4$ GeV^2, and for x_B of the order of 0.35 (valence quarks).

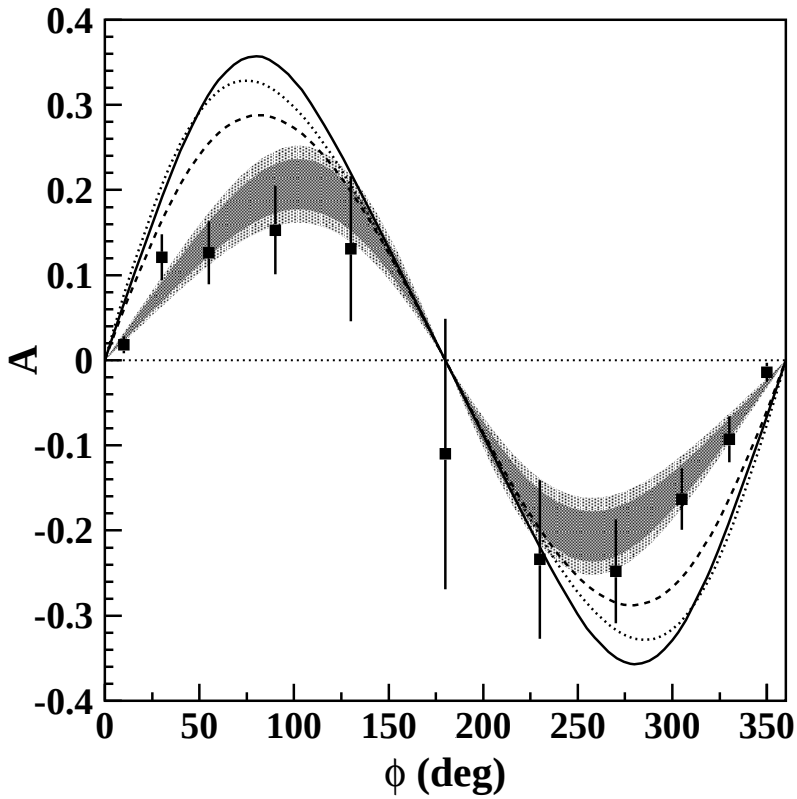

Figure 6: ϕ dependence of the $ep \rightarrow ep\gamma$ Beam Spin Asymmetry at 4.25 GeV [3]. Data are integrated over the range of Q^2 from 1 to 1.75 GeV^2, x_B from 0.13 to 0.35 (with the condition $W > 2$ GeV) and $-t$ from 0.1 to 0.3 GeV^2. The shaded area is the fit to the function $\alpha \sin\phi + \beta \sin 2\phi$. The curves are from Refs. [10, 22, 24].

4.2.1 Hall B - E99-105

Experiment 99-105 [26] was a major component of the E1-6 run with CLAS in fall 2001. It was the first experiment to run at 5.75 GeV beam energy. Its first goal was to measure the Q^2 dependence of the $ep \rightarrow ep\rho_L, (\omega_L, \phi_L)$ reactions, and to test the underlying s-channel helicity conservation (SCHC) hypothesis. While the handbag contribution does not appear to dominate the ω channel at JLab kinematics [27], the ρ channel may be qualitatively described by the GPD formalism [28]. Results from E1-6 on the ρ and ϕ channels will be available soon.

An analysis of $ep \rightarrow epX$ events from this run is also in progress. The method used in [3] may not be used anymore because of the decreasing missing mass resolution at higher beam energy. However, at small values of $|t|$ and with the use of a Monte Carlo to estimate the contamination of $ep \rightarrow ep\pi^0$ events, beam asymmetries could be obtained for the $ep \rightarrow ep\gamma$ process. Furthermore, the total number of events is large, allowing for the first time a two-dimensional binning (Q^2 and x_B dependences, or x_B and t). The present proposal is a major improvement with respect to E1-6, ensuring full exclusivity with the detection of three particles, and with an increased integrated luminosity.

4.2.2 Hall A - E00-110 and E03-106

Experiments E00-110 [29] and E03-106 [30] were performed in the fall 2004. The DVCS beam spin asymmetries and cross section differences will be determined at three Q^2 intervals, for a fixed interval of x_B, both for proton and for neutron targets, the latter in considering the quasi-free DVCS process on the deuteron. These experiments will provide a precise check of the Q^2 dependence of the $eN \to eN\gamma$ cross section differences (for different beam helicities). Our proposal has an overlap with E00-110, but is directed toward a much larger kinematical coverage, extends to higher Q^2, and explores the x_B and t dependencies. A more detailed comparison with E00-110 was presented in the Appendix of our initial proposal. In summary, the data from this experiment is expected to be divided in 372 bins in (Q^2, x_B, t, ϕ), each with only 25% (in average) less counts than in each of the 48 bins anticipated in Hall A.

4.2.3 Hall-B - E05-114

Experiment E05-114 [31] will measure DVCS target spin asymmetries using CLAS with its longitunally polarized target and the new inner calorimeter developed for E01-113 and the present proposal. That experiment was approved with priority A at PAC28. Target and beam spin asymmetries provide different linear combinations of GPDs, the former having an enhanced sensitivity to $\tilde{H}$. The use of both observables, with their anticipated high statistical precision and kinematical dependences, will give a handle for the separation of different GPDs. In E01-113 and its presently requested continuation, the acceptance for DVCS events is significantly larger because of the optimized magnet configuration.

4.3 Experiments at HERA

4.3.1 HERMES

HERMES published its first beam polarization asymmetries for $\vec{e}p \to e\gamma X$ [32], which, in the missing mass region around the proton mass, also point to a characteristic $\sin\phi$ dependence attributed to BH-DVCS interference. Other interesting DVCS observables were investigated as well: beam charge asymmetries, target spin asymmetries (both longitudinal and transverse), for which preliminary results have been shown. Generally speaking, these results suffer from rather low statistics. Moreover, the final state baryon is not unambiguously constrained to be a proton (Δ's and possibly other baryon resonances may contribute to the measured signal). It may be hard to extract from these measurements a truly exclusive DVCS signal. The HERMES collaboration has built and is currently installing a recoil proton detector to remedy this situation. Though HERMES is operating at lower luminosity than CLAS, the new generation experiments there will be in direct competition with the present proposal.

4.3.2 H1 and ZEUS experiments

Using also $ep \rightarrow e\gamma X$ events, but in this case with the HERA colliding beams, H1 [33, 34] and ZEUS [35] were able to extract DVCS cross sections, after a subtraction for non-exclusive $ep \rightarrow ep\gamma$ events relying on simulations. For lack of statistics, the data in both cases were integrated over ϕ. This integration cancels most of the interference term, allowing for a subtraction of the calculable BH contribution. The data are also integrated over a wide kinematical region, $4 < Q^2 < 80$ GeV^2, $40 < W < 140$ GeV and $|t| < 1$ GeV^2 (although the latest results [34] allow an exploration of the t dependence). The results are in reasonable agreement with NLO QCD predictions using parameterizations of GPDs in the gluon sector. Indeed, because of the very small values of x_B, it is mainly the nucleon gluon content which is probed, and this has hardly any overlap with the present proposal. Here again, new measurements are in progress with the recently added "Very Forward Proton Spectrometer" in order to detect the proton in the final state.

4.4 CERN experiment

A dedicated DVCS experiment at CERN is being studied for the COMPASS detector [36]; it is not expected to run before 2010. It would use the 200 GeV muon beam from the SPS and the COMPASS set-up augmented by a specially designed proton recoil detector. The high beam energy ensures that the DVCS process dominates over the Bethe-Heitler contribution. It is planned to use a combined beam spin and beam charge asymmetry to reach an increased sensitivity to different GPD parameterizations. The range of x_B values (0.02 to 0.25) would connect the gluon and the (valence) quark sectors. In spite of the high energy, the low luminosity limits the measurements to values of Q^2 only slightly higher than this proposal.

Figure 7 illustrates the kinematical coverage of these experiments. It shows the broad interest at many laboratories to measure the DVCS process as a means of accessing the GPDs. In the short term, CEBAF with its 6 GeV beam can contribute uniquely to exploratory measurements of deep exclusive reactions, and of DVCS in particular.

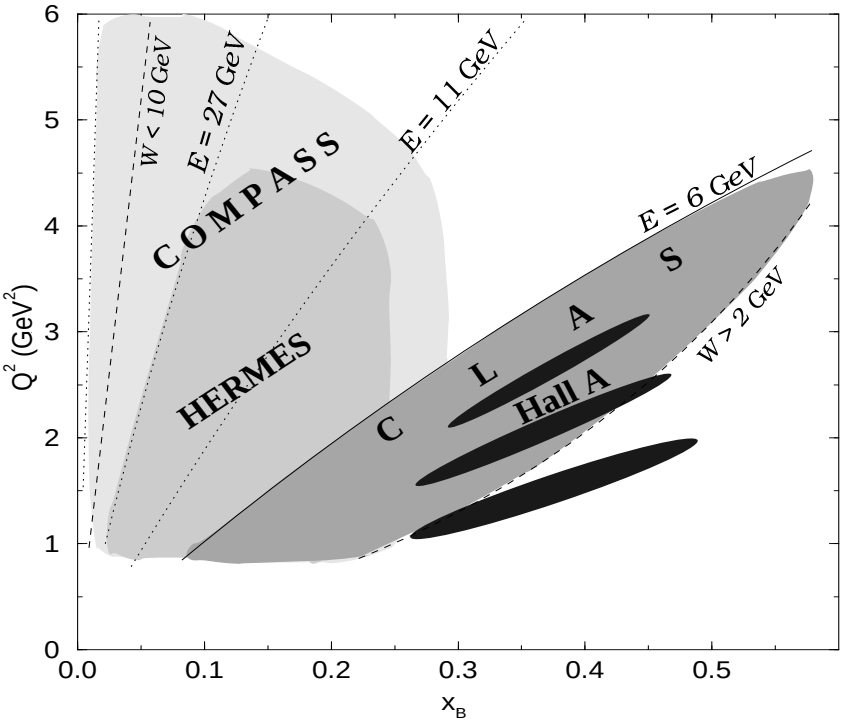

Figure 7: Kinematical coverage for various existing or proposed DVCS experiments.

5 Experiment E01-113

A dedicated DVCS experiment in Hall B was approved by JLAB PAC-20 with "A" rating, E01-113. The goals of the experiment are the measurement of the t and x_B dependence of beam spin asymmetry for several Q^2 bins and the extraction of the helicity-dependent cross section difference in the reaction $ep \rightarrow ep\gamma$. As CLAS covers a broad kinematical range, we will be able to test the Q^2 dependence of the DVCS process for different x_B. This will test whether we are in a regime where a direct interpretation of the results in terms of GPDs is possible.

The first part of the experiment was completed during March-May of 2005. We used a 5.75 GeV longitudinally polarized electron beam with an average polarization of $\sim 80\%$, incident on the 2.5 cm long liquid hydrogen target. A total of 10^9 electron events were collected during 36 beam days of running. As a trigger for the data acquisition of CLAS, the coincidence signal of the forward electromagnetic calorimeter (EC) and the Cherenkov counter (CC) was used. We were able to collect about 43% of the total required data for the beam spin asymmetry measurement. In Fig. 8, the kinematical coverage in Q^2, x_B, and t for reconstructed electron-proton pairs from the preliminary analysis of the collected data is shown. The data cover the kinematical range proposed in the experiment E01-113.

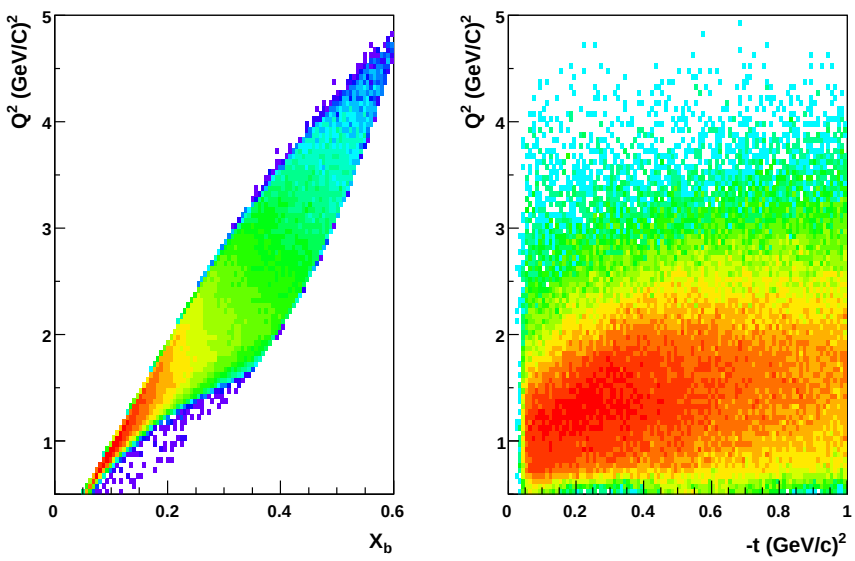

Figure 8: The Q^2, x_B, and t coverage during the spring 2005 DVCS run with CLAS at 5.75 GeV beam energy.

5.1 CLAS configuration during the Spring 2005 run

Important conditions for running the experiment E01-113 were the luminosity of

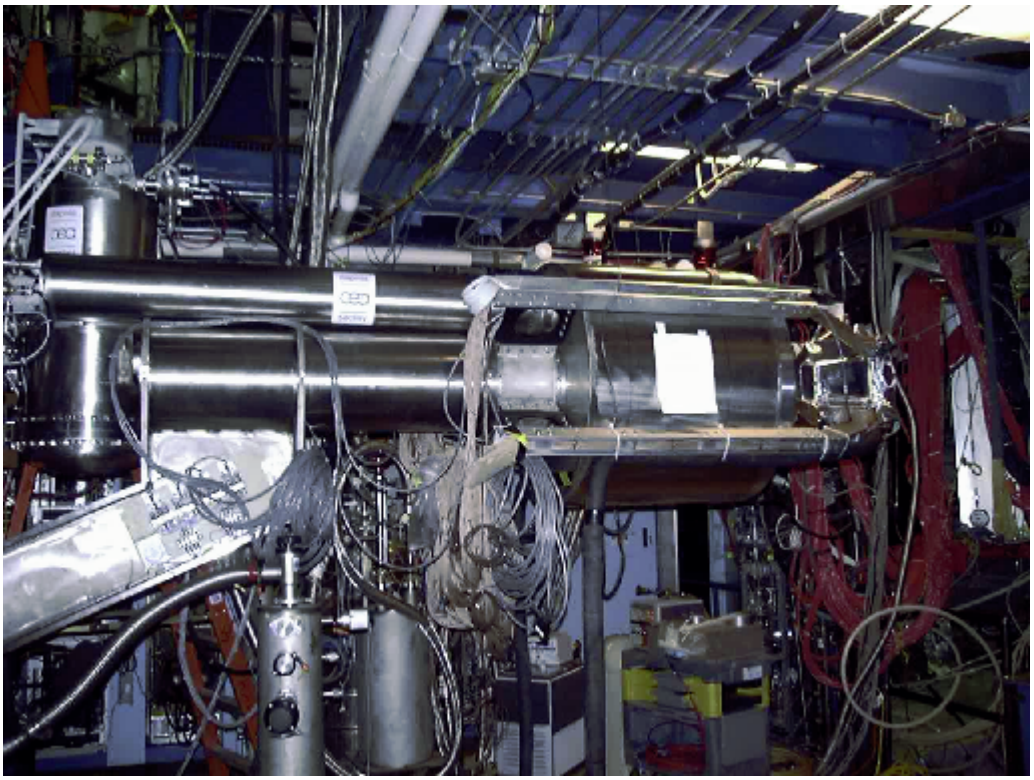

Figure 9: New superconducting solenoid magnet and 424 channel $PbWO_4$ crystal calorimeter on the insertion cart in the Hall. Operational current for the solenoid is 534 A, max longitudinal field 4.7 T.

2×10^{34} $cm^{-2}sec^{-1}$ and the detection of the DVCS photons at very small angles. These required the following changes to the standard CLAS configuration:

1. The target was moved to 67 cm upstream of the CLAS center.
2. A new superconducting solenoid magnet was used to shield the CLAS drift chambers (DC) and new IC (see below) from Møller electrons.
3. A new 424 channel lead tungstate ($PbWO_4$) crystal calorimeter, inner calorimeter (IC), was installed for the detection of high-energy photons in the angular range from 4 to 16 degrees.
4. The lead shielding pipe was redesigned to absorb the electromagnetic background behind the crystal calorimeter.

The DVCS collaboration built, installed, and commissioned two new devices in Hall B: a superconducting solenoid magnet and a 424 channel $PbW0_4$ crystal calorimeter (Fig. 9). Both devices were critical for the running of this experiment and both devices showed excellent performance during the run.

5.2 Superconducting solenoid magnet

A superconducting solenoid magnet was designed and built at Saclay (France) for the DVCS experiment. The magnet was designed to have optimal shielding capability for Møller electrons produced in the beam-target interactions, an open bore and a wide opening angle for scattered particles (up to 60°), while minimizing the forces on the CLAS torus. Besides the main coil the magnet has also a compensation coil that runs reverse current. It allowed the suppression of the field strength away from the solenoid magnet center, lowering the forces on the torus coils.

This new solenoid magnet was installed in Hall B during February-March of 2005. The forces on the torus were measured and found to be in the acceptable range for the regime of the standard operations. At the full current setting of the solenoid, we were able to run the torus at 54% of its maximal current, which was anticipated and acceptable for this experiment. The overall stability and reliability of this new superconducting solenoid magnet was excellent throughout the run.

With the solenoid magnetic shield for Møller electrons, we ran the major part of the experiment at a luminosity of 2×10^{34} cm^{-2}s^{-1}. The contribution of the hydrogen target was 80% of that. The luminosity was somewhat lower at the beginning of the run, mainly due to beam instabilities and induced large DC current.

5.3 $PbWO_4$ crystal calorimeter

The second new device that was used in this run was a 424 channel lead-tungstate crystal calorimeter (IC). The device was designed, constructed, and commissioned by ITEP (Moscow), Orsay (France), Saclay (France), and JLab groups. In Fig. 10, a view of the calorimeter, crystals and the readout electronics fully assembled, is shown. Each channel consists of a tapered $PbWO_4$ crystal (16 cm long, 1.3×1.3 cm^2 section in front, 1.6×1.6 in the rear end), an APD for the light read out, and a specially designed pre-amplifier. The output of the pre-amplifier was split into two in order to measure both the amplitude (ADC) and the time (TDC) characteristics of the signal.

This calorimeter design benefited from R & D done for CMS at LHC [37], but it was the first time a $PbW0_4$ crystal calorimeter with APD readout was operated in a real experiment. The IC was positioned at 57 cm downstream of the target. The angular range for the detection of photons was from 5 to 15 degrees. The overall operation of the calorimeter was very successful. Only 2 channels out of 424 failed to operate at the end of the experiment. On-line and off-line monitoring, calibration, and reconstruction tools allowed for fast feedback for the hardware correction and the data quality checks.

To maintain stable operations of the calorimeter, constant light output of crystals, and fixed gains of APDs, the temperature inside the calorimeter had to be kept stable with very high accuracy. The calorimeter box and frames holding the crystals were designed to handle the temperature stabilization. In Fig. 11, readings of several

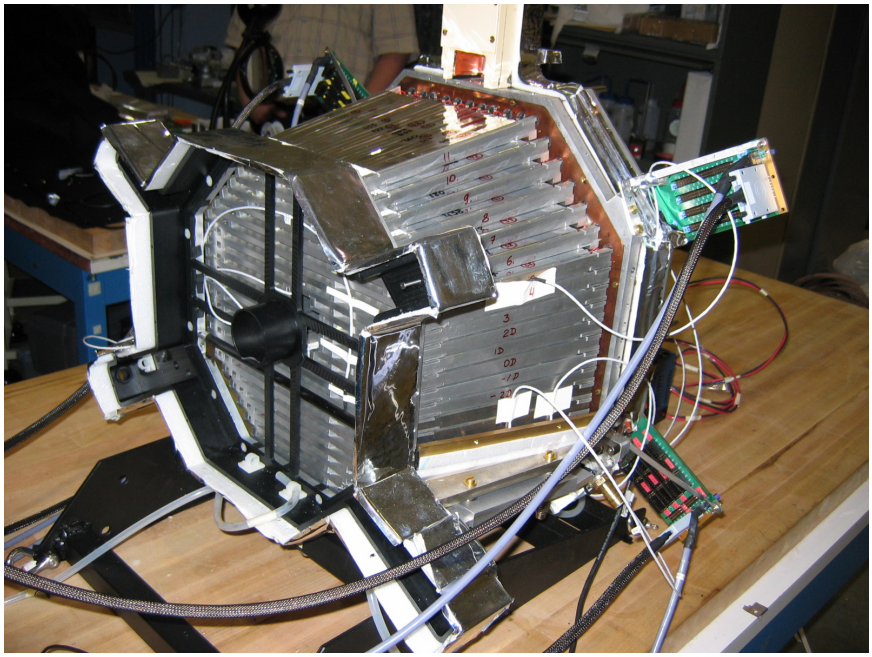

Figure 10: View of the calorimeter.

temperature sensors inside the calorimeter are shown for an 18-day period. The temperature stability of the system is well below the goal limit of 0.1°C.

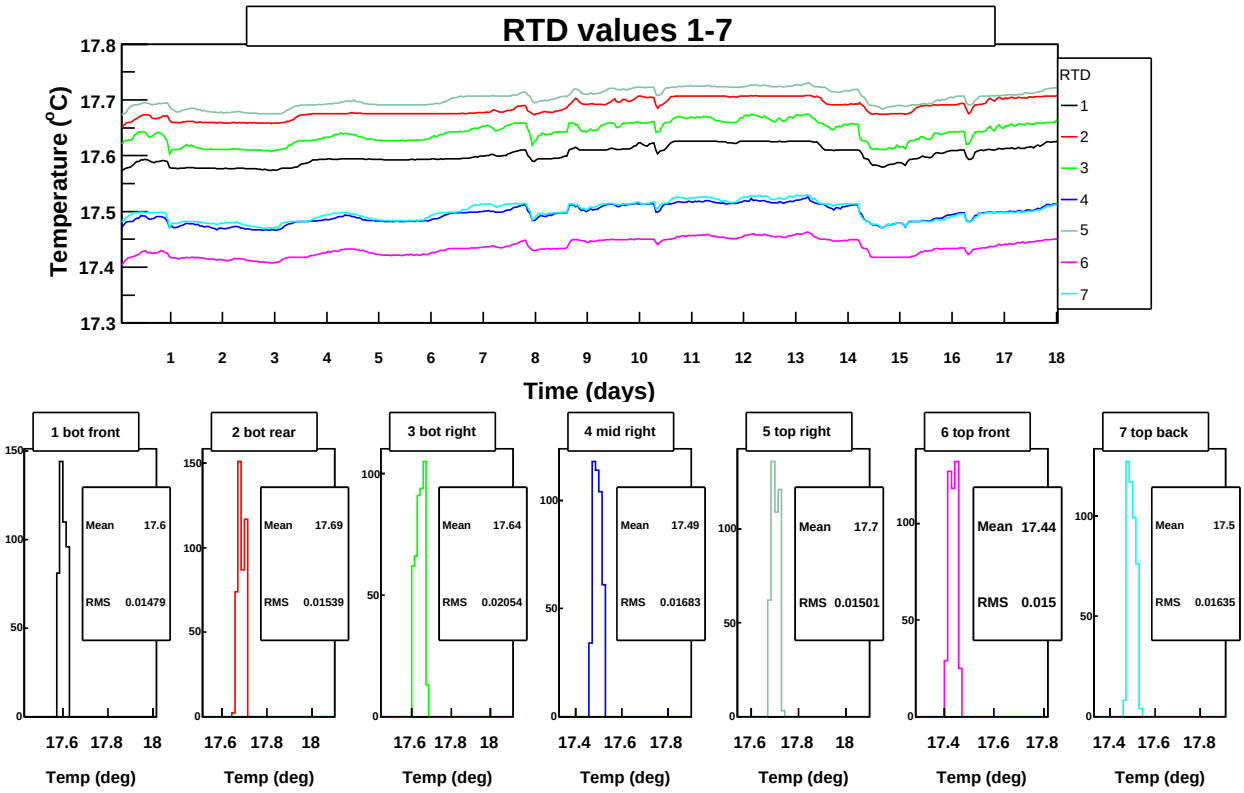

Figure 11: Temperatures inside the calorimeter. Top plot: temperatures shown by RTDs as a function of time. Bottom plots: temperature spreads during 18 days.

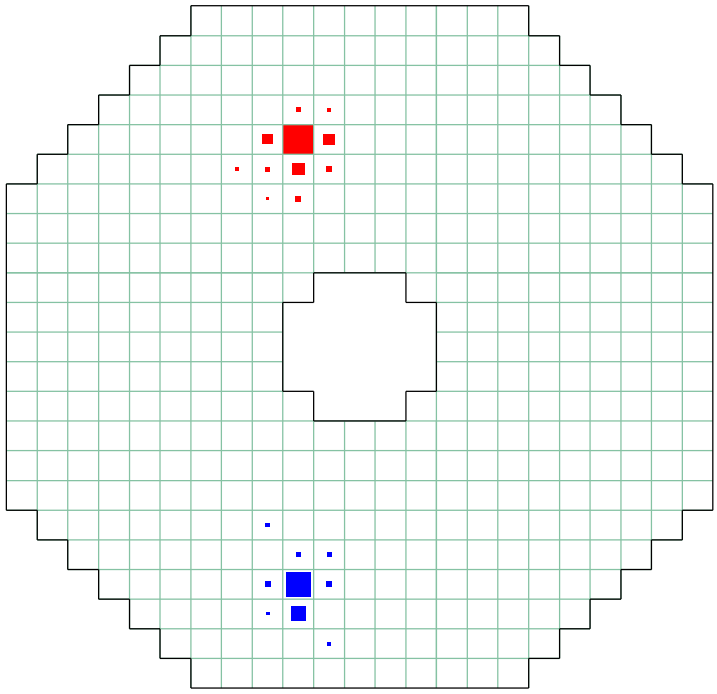

Figure 12: Single data event showing 424 channel calorimeter view with two clusters of deposited energy. Clusters are shown with different colors. The size of the shown hits is weighted with hit energy.

5.3.1 Performance of the calorimeter

The main purpose of having a calorimeter at small angles is the direct detection of the DVCS photons and separation of the DVCS and π^0 events. This requires good energy resolution of the calorimeter. In the initial proposal, we were aiming for a < 7 % energy resolution at 1 GeV. Several steps were made to achieve the required energy resolution. First the APD gains were set using the laser calibration system. Then preliminary gains were determined using elastic electrons scattered in the angular range of the calorimeter. The final adjustments were done using π^0 events collected in special runs using an IC trigger. For the selection of neutral pions, events with two reconstructed clusters were analyzed (Fig. 12). The gains of each channel were adjusted using the pion mass as a constraint in the invariant mass distribution of two clusters, assuming that these clusters are photons.

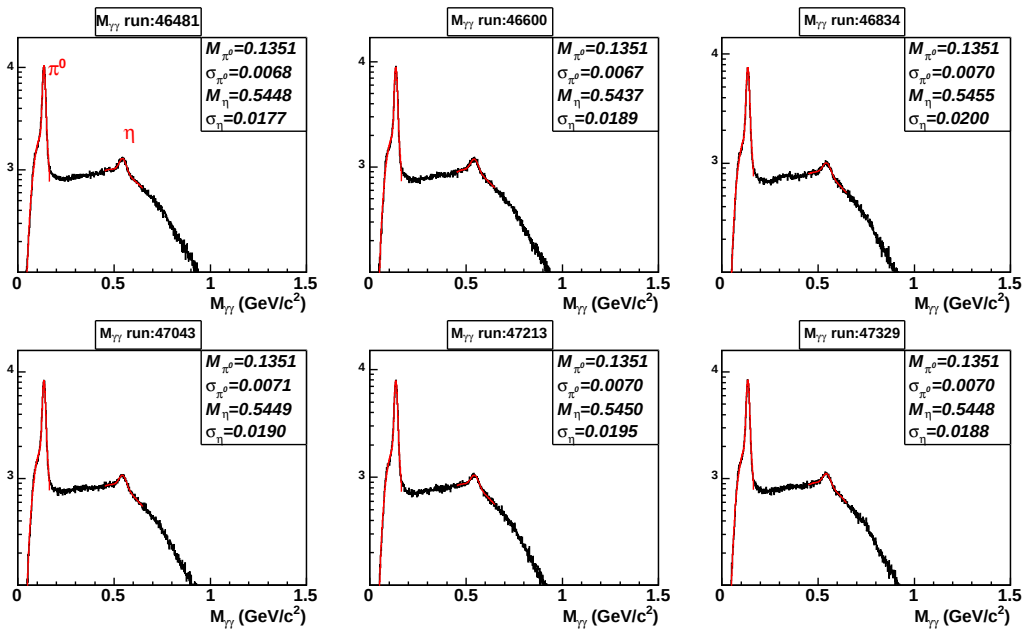

Figure 13: IC energy calibration results [38]. Invariant mass of reconstructed two photons from 6 calibration runs. π^0 and η peaks are fitted with a sum of Gaussian and a third order polynomial function.

In Fig. 13, the invariant mass distributions of two photon clusters are shown for six calibration runs taken during the whole run. Peaks corresponding to the π^0 and η events are clearly visible. The achieved mass resolution of 7 MeV (σ) for the π^0 is what was expected from the GEANT simulations.

The time information of IC was calibrated as well. In Fig. 14, the time difference between the IC hits and the CLAS trigger is shown. The distribution in the left graph of the figure is when all CLAS triggers are considered, while for the right graph the CLAS trigger is required to correspond to a good electron identification and track. After selection of the electron events, there is hardly any background in the time distribution of CLAS-IC. The time resolution of the IC is of the order of 0.7ns, dominated by the TDC channel width of 0.5 ns. This will help to reject the few remaining accidental events in the CLAS-IC coincidence.

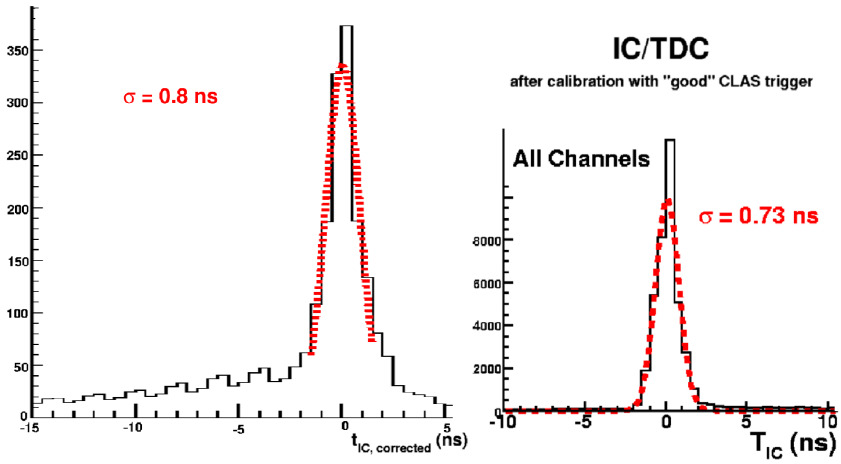

Figure 14: IC TDC calibration results [39]. Left plot: CLAS trigger - IC coincidence spectrum, for all IC hits, after CLAS track flight time correction and IC time-walk correction. Right plot: same, but with the additional requirement that the CLAS trigger corresponds to a good electron.

5.3.2 Event reconstruction with CLAS

The reaction $ep \rightarrow ep\gamma\gamma$ is used to check the status of the event reconstruction using CLAS and IC. For studies of the energy and angular resolutions of IC $ep \rightarrow ep\gamma\gamma$ events are used, for which the electron and the proton are detected in CLAS and the two photons in IC. The $ep \rightarrow ep\pi^0$ events were selected using cuts on the missing mass of the (ep) system and the invariant mass of the two photons (see Fig. 15).

In the selected event sample, the pions are in the energy range from 2 to 5 GeV (see top left graph in Fig. 16). The difference of the calculated, using the kinematics of the electron and the proton, and reconstructed in IC energies is shown in the top right plot of Fig. 16. The lower graphs of the figure correspond to the difference of the calculated and reconstructed angles.

The results of the energy resolution studies are shown in Figure 17. The energy difference described above was fitted with a Gaussian in several energy bins. The dependence of the energy resolution on energy is shown in the lower plot of Figure 17 (dark points). The red line on the graph is the fit to these points using the function:

$$\frac{\sigma}{E} = \frac{a}{E} \oplus \frac{b}{\sqrt{E}} \oplus c \tag{9}$$

where the sum is quadratic and a, b and c are the fit parameters. The fit resulted in $a = 0.053$, $b = 0.035$, and $c = 0.017$ [38]. The blue line on the graph is the same function as in Eq. 9 with the value of parameters a, b, and c from the simulations [40]. One should note that in the presented energy difference the CLAS resolution also contributes and that the full calibration of CLAS is still underway.

From the lower plots of Fig. 16 the average angular resolution for the polar angle is ~ 5 mr and for the azimuthal angle ~ 20 mr. We expect these numbers to improve significantly after the final calibration of the CLAS drift chambers and the tuning of the tracking in the region of the high magnetic field of the solenoid. The intrinsic IC position resolution, as estimated from simulations [40], is expected to be (in mm):

$$\sigma \simeq \frac{1.8}{\sqrt{E}} \oplus 0.1 \tag{10}$$

which corresponds to about 5 mr at 1 GeV for a point target.

5.4 Measurement of radiation damage in IC

In anticipation for a long term operation of the inner calorimeter, radiation damage was both simulated beforehand [41] and measured during the spring 2005 run. For this purpose, pedestal runs were taken with beam on, and the excess energy above the pedestal peaks analyzed and translated into radiation dose. The results for the central part of IC are illustrated in Fig. 18. The observed distributions are in reasonable agreement with simulations. The inner ring crystals are obviously the most subject

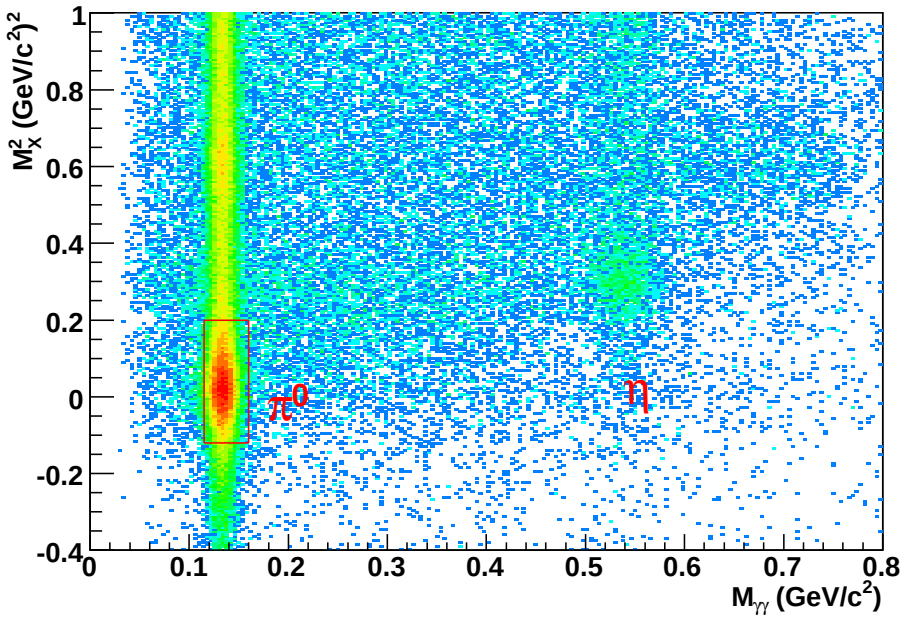

Figure 15: Selection of $(e, e'p\pi^0)$ events. $(e, e'p)$ missing mass squared vs invariant mass of two photons detected in IC with electron and proton detected in CLAS. The red box indicates the cut for selecting π^0s.

to radiation, at a level approaching estimates for LHC/CMS operation. Only for these did we observe a few percent decrease of signal output over the whole run period. We can then operate the inner calorimeter for new and longer periods of time at this luminosity.

5.5 Status of the data analysis

Currently, the collaboration is in the final stage of adjusting the calibration of all detector subsystems. The new crystal calorimeter, IC, is fully calibrated and the reconstruction algorithm is tested [38]. Charge particle identification in CLAS using time-of-flight is in reasonable shape, see Figure 19. Considerable efforts are devoted on improving the tracking in the presence of the strong solenoidal field around the target, where there is no track position information available. Already at this stage we are able to clearly see the thin target foils in the empty target runs, Figure 20. By the end of 2005, we will start the final processing of the data. It will take about two months to reduce the data in a form ready for physics analyses.

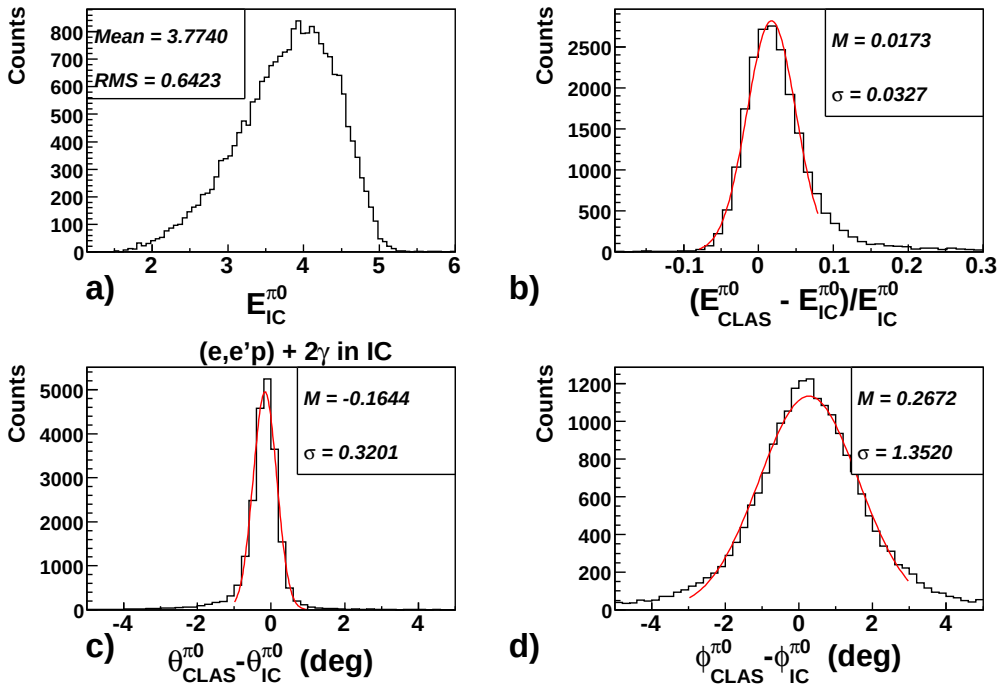

Figure 16: Inner Calorimeter resolution studies. a) π^0 energy distribution. b), c) and d) energy, θ and ϕ angle resolutions, respectively.

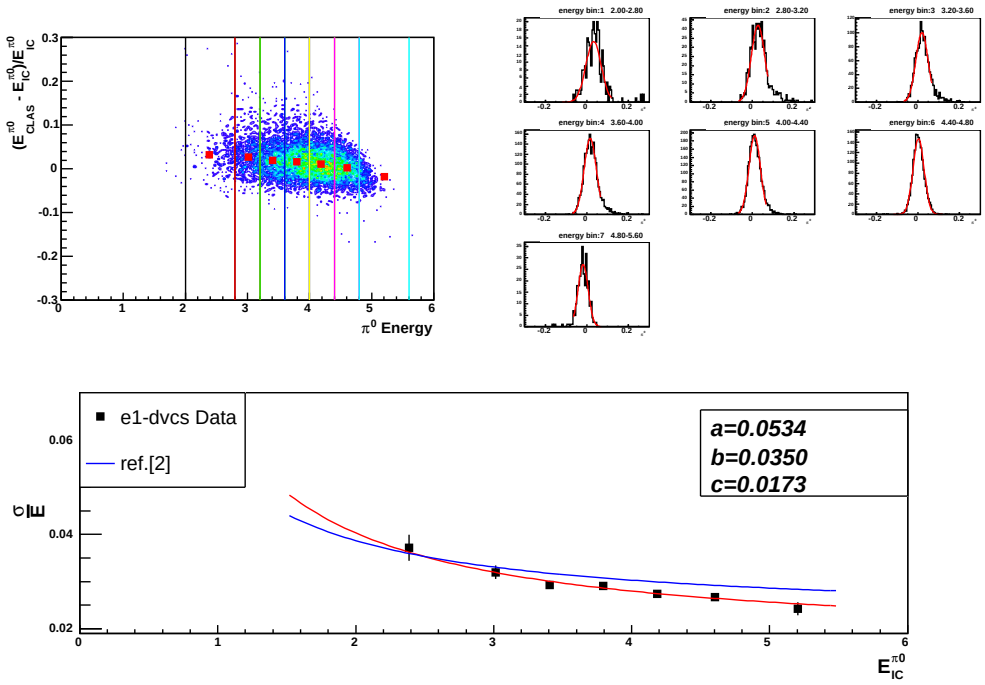

Figure 17: Dependence of Inner Calorimeter energy resolution on E.
Top left: $\Delta E/E = (E^{\pi^0}_{CLAS} - E^{\pi^0}_{IC})/E^{\pi^0}_{IC}$ vs energy of the π^0. The vertical lines indicate the energy slices. The red points are mean values of the Gaussian fit.
Top right: ΔE/E slices fitted with a Gaussian.
Bottom: σ/E values of the fit as a function of energy fitted with $\frac{a}{E} \oplus \frac{b}{\sqrt{E}} \oplus c$ function. The blue curve is an estimate from [40].

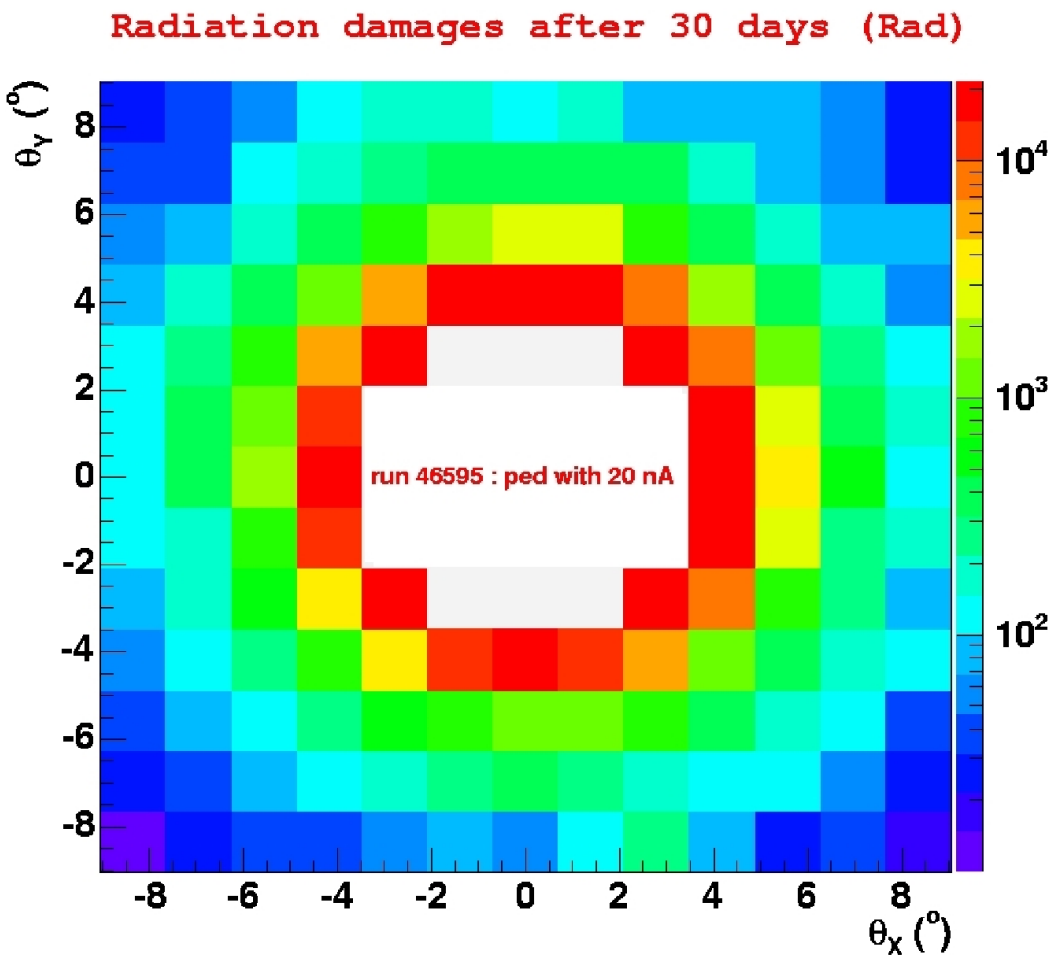

Figure 18: Radiation dose, in rad per hour, for the central part of IC. Each square corresponds to an IC crystal.

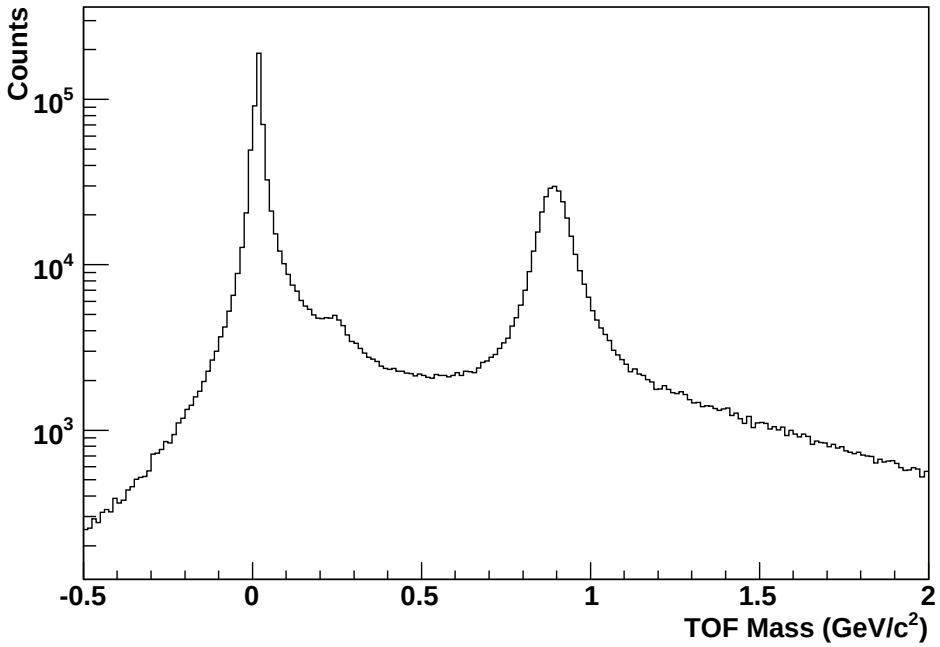

Figure 19: The mass squared for positively charged particles calculated using the time-of-flight information from SC and the momentum reconstructed in DC.

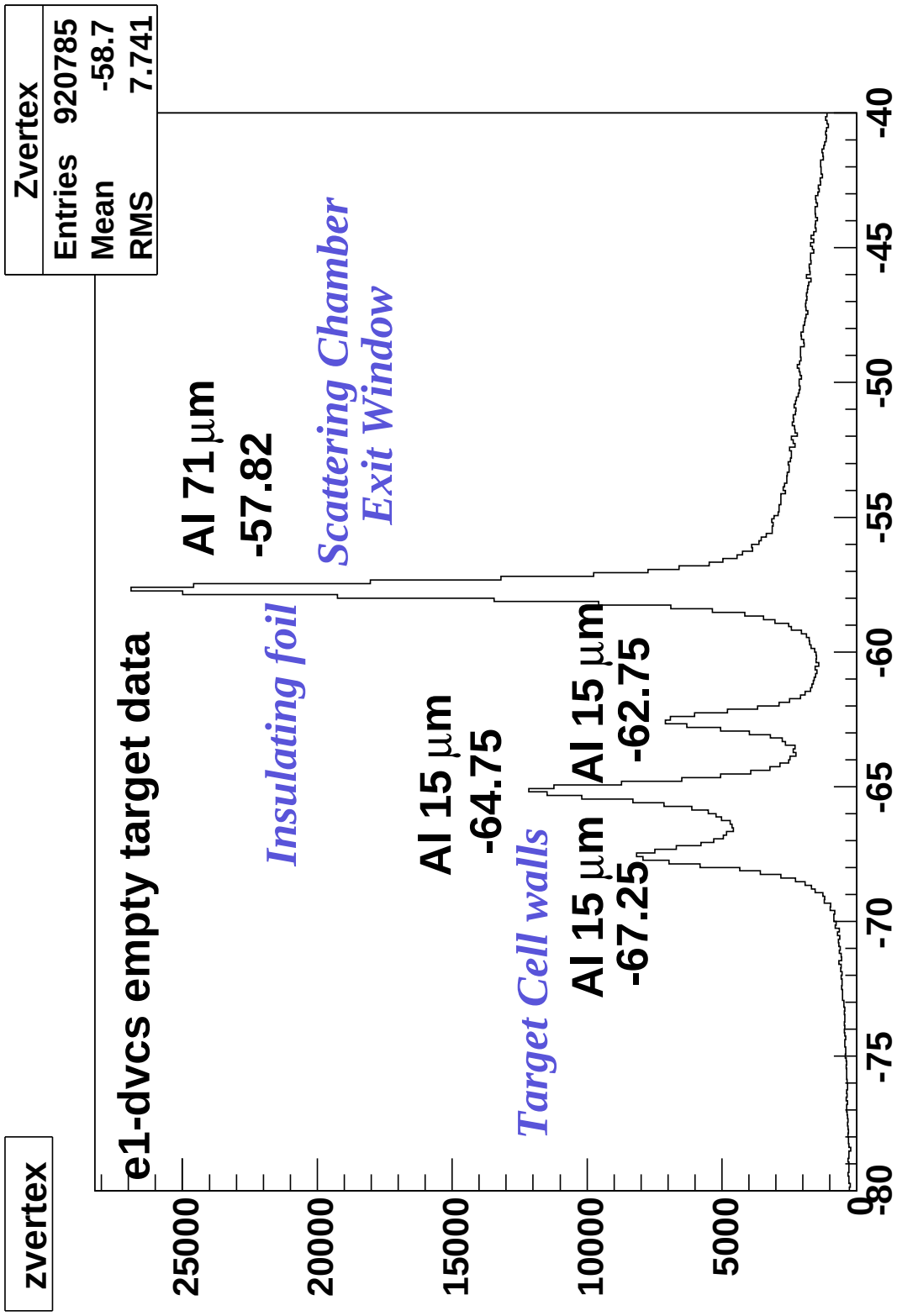

Figure 20: Vertex position for the electron along the beam direction reconstructed in analysis of the empty target runs.

6 Event identification and reconstruction

The event identification in CLAS is accomplished using charged particle tracking in the magnetic fields (from both torus and solenoid), time-of-flight, and momentum information. Electrons are separated from heavier particles using threshold gas Cherenkov detectors, and electromagnetic calorimeters.

Electron and proton momenta are reconstructed in the CLAS drift chamber system using the standard CLAS software. For the proposed dedicated experiment, photons from direct production and from π^0 decays (or from η decays) will be reconstructed using the new small angle photon detector (IC) and the CLAS forward angle EC. This will provide large acceptance coverage for both reactions.

The reaction $ep \rightarrow ep\gamma$ can, in principle, be identified through the determination of the missing mass M_X in the reactions $(ep\gamma X)$ and (epX). This method was used successfully in the analysis of the 4.25 GeV data [3]. However, the missing mass resolution achieved in CLAS is not good enough to have a separation of the $ep\gamma$ and $ep\pi^0$ final states event by event. We therefore used a technique that analyzes the line shape of the missing mass distribution to separate the two contributions. The systematic error estimated for the resulting DVCS/BH asymmetry is considerably larger compared to the direct detection of photons.

For the dedicated run at 6 GeV, and with much higher statistics, the detection of photons in the CLAS EC and in IC is mandatory and will allow the separation of single photons from π^0's event by event. We estimate that up to momenta of 5 GeV, a maximum of 2% of π^0's could be mistaken as single cluster photon events [40]. Rejections of π^0's from a shower profile analysis will work to higher momenta, but this is not required for this experiment.

The simulation used below for estimates of physical background contamination and of acceptances is the one used in proposal E01-113. With our present knowledge of the CLAS/DVCS detector configuration, it is being improved, but this initial version is sufficient here for our purpose. Also, since the achieved resolutions in IC are better than in our initial proposal, the background estimates hereafter may be considered as upper limits.

Separation of single γ from $\gamma\gamma$ events.

Accidental coincidences do not play any significant role in electron scattering experiments with CLAS because of the low luminosity and the good time resolution. The main sources of background to the $ep\gamma$ final state will be from $ep\pi^0$ and from $ep\gamma\gamma$ events, where only one of the two photons is detected. The former process will be measured directly for the same kinematics as the $ep\gamma$ process, and can be subtracted. The latter reaction corresponds to hadronic production of two photons, which can be measured in the experiment, or inelastic radiative corrections. The latter ones are dominated by processes when the incoming electron radiates off a photon (which escapes detection in the beam pipe) and e.g. N^* resonances are excited,

which subsequently decay into a proton and a photon. The electromagnetic decay is suppressed by typically two orders of magnitude in comparison to a hadronic process, and the invariant mass of the $\gamma\gamma$ final states results in a broad range in the epX missing mass. Most of these events will be eliminated by missing mass cuts. However, the usual radiative corrections are needed to determine the unradiated cross section.

To be more definite, we simulated the following processes: $ep \to ep\gamma$, $ep \to ep\pi^0$, $ep \to ep\gamma\gamma$, where we assumed a $1/Q^4$ and e^{-4t} behavior for the Q^2 and t dependences of the cross sections, respectively. The ϕ-modulation was simulated according to the CLAS DVCS data at 4.2 GeV. The final state $ep\gamma\gamma$ was generated according to a double emission of photons, randomly distributed according to the same t-dependence, and according to the radiative process with subsequent excitation and decay of excited states. The detection probability for both photons from the π^0, the direct $ep\gamma\gamma$, and radiative $ep\gamma\gamma$, is 0.55, 0.50, and 0, respectively. The latter reaction (inelastic radiative correction), which cannot be measured directly, has a small detection probability for the non-radiative photon (see last column in Table 1). It is the main part of the inelastic radiative corrections.

The use of a combination of the epX and $ep\gamma X$ missing masses allows the isolation of single photon as well as π^0 events. This is described in Fig. 21. It shows the efficiency for the detection of single photons, and the probability for the rejection of π^0 events. The results are summarized in Table 1, where E_X is the cut on the missing energy as in Fig. 21. Complete kinematical fits will further improve this separation. For example, one can also make use of the required co-planarity for the direct $\gamma^*\gamma p$ events, while $\gamma^*\gamma p$ from $ep\pi^0$ events will generally not be co-planar.

Table 1: Simulated $ep\gamma$ configurations (detection of an electron, a proton and a single photon) from various processes. The numbers correspond to the ratios $N_{ep\gamma}/N_{ep}$, separately for each individual process. These ratios are given for two different values of the E_X cut.

$ep \to$ E_X(GeV)	$ep\gamma$	$ep\pi^0$	$ep\gamma\gamma$ (direct)	$ep\gamma\gamma$ (radiative)
0.2	0.65	0.04	0.06	0.005
0.4	0.7	0.07	0.1	0.01

In kinematical areas where the π^0 yield is much smaller than the photon yield, for example in the angle range below 3 degrees, which is not covered by calorimetry, the missing mass method may still be an effective way of measuring the beam spin asymmetry, although we are not counting on using this part of the phase space.

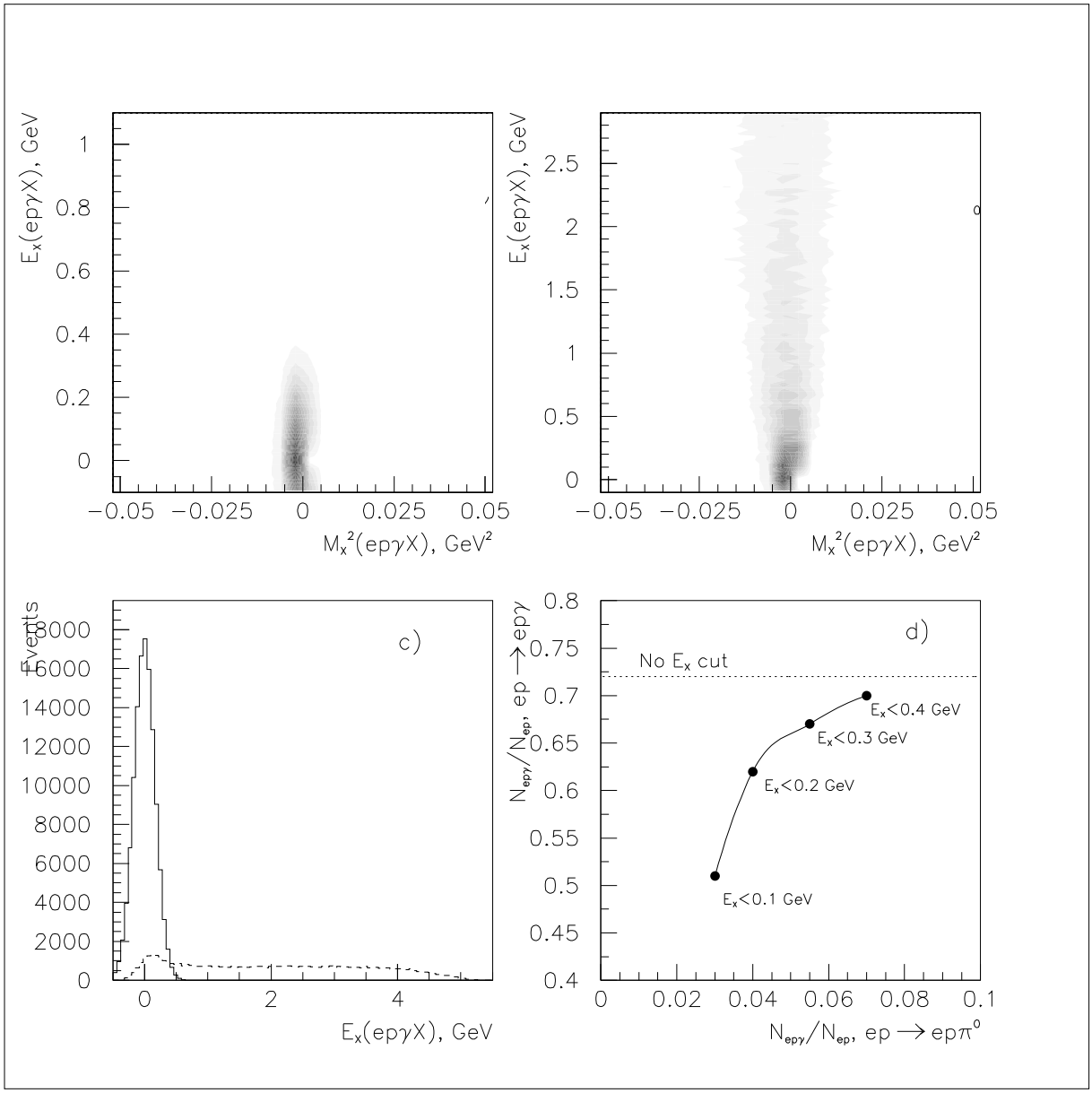

Figure 21: Separation of $ep\gamma$ and $ep\gamma(\gamma)$ events using the missing mass and missing energy method. The top panels show the missing energy from $ep\gamma$ (left) and $ep\pi^0$ (right) events if only one photon is detected versus missing mass for $ep\gamma X$. The projection of both graphs is shown at the bottom left. The π^0 contamination is a small fraction under the single photon peak. The bottom right panel shows the probability for a π^0 to be misidentified as a single photon on the horizontal axis and the single photon detection probability on the vertical axis a function of the missing energy cut.

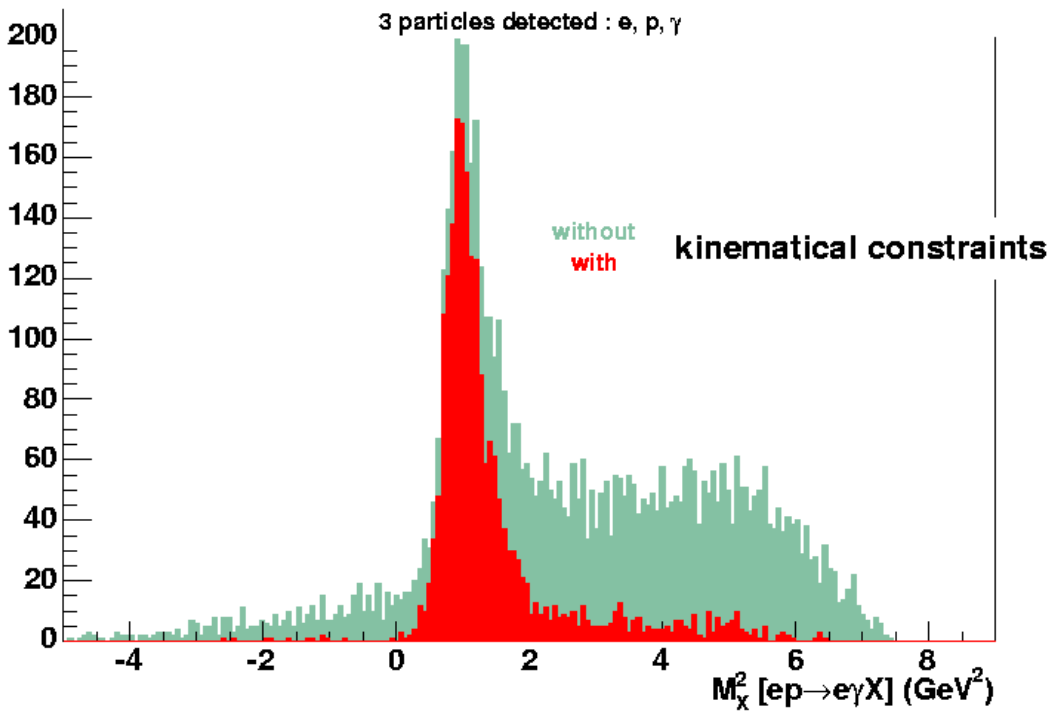

Figure 22: The missing mass distribution of $(e\gamma)$ from preliminary analysis of the $ep \to ep\gamma X$ using small sample of data. The green histogram corresponds to all events. Red histogram is after using kinematical constraints on missing P_X, P_Y, and P_Z.

Preliminary analysis of data

Some preliminary analyses of spring data for the event identification, using not fully calibrated data, are already started. In Figure 22 the missing mass distribution of $e\gamma$ in the reaction $ep \to ep\gamma X$ is plotted without (green histogram) and with (red histogram) cuts on X, Y, and Z components of the missing momentum. No cut on the missing energy is applied. Although, this kinematical constraints does not tell what is the shape of the π^0 background under the peak, it clearly reduces the π^0 background by many orders.

7 Count rates and statistical errors

The expected number of counts is given by

$$N = \mathcal{L} \times \text{time} \times \sigma \times (\Delta Q^2 \cdot \Delta x_B) \times \Delta t \times \Delta\phi \times (\Delta\varphi_e)_{\text{eff}}/2\pi \tag{11}$$

With the optimized configuration as described in Sec. 5, a luminosity of 2×10^{34}

$cm^{-2}s^{-1}$ can be achieved. For 60 days of beam time, this corresponds to an integrated luminosity $\mathcal{L} \times \text{time} = 10^8$ nb^{-1}.

The cross sections are calculated following Refs. [10, 22], using the ξ-dependent parameterization of the GPDs. These calculations are valid to leading order for the handbag diagram and include the interference with the Bethe-Heitler process.

In a large acceptance detector like CLAS, the binning of the data according to the relevant kinematical variables is somewhat arbitrary. For the sake of presentation in a table and in figures, we have chosen here rather wide bins. It is very likely that the final data set will be subdivided into finer bins, for a better study of the Q^2, x_B and t dependences of the observables.

- The Q^2 and x_B bins are indicated in Table 2. The resulting area $(\Delta Q^2 \cdot \Delta x_B)$ is smaller than the product $\Delta Q^2 \times \Delta x_B$ because of limitations in the electron scattering angle and of the requirement $W > 2$ GeV (see Fig. 8).

- The t range will be divided into three or four bins, taking into account the increasing value of $|t_{min}|$ at large (Q^2, x_B). The binning in $|t|$ will be the following: $(0.1 - 0.25)$, $(0.25 - 0.40)$, $(0.40 - 0.60)$ and $(0.60 - 0.80)$.

- The whole ϕ range will be divided into 12 bins of 30°.

This procedure would result into a total of 372 bins for the whole data set.

For the acceptance $(\Delta\varphi_e)_{\text{eff}}/2\pi$, we used averaged values (over ϕ and t). The corresponding numbers in Table 2 are good to 15-20%, with this initial version of the simulation.

The resulting numbers of counts in Table 2 may appear large, but we reiterate that they correspond to bins much wider than desirable for our study. Also the cross sections at $\phi = 180°$ are significantly smaller (see Fig. 25). These numbers are used to calculate the statistical uncertainties illustrated in the figures of the following section. A beam polarization of 0.75 is assumed for the calculation of $\Delta(BSA)$.

7.1 Systematic errors

The proposed spin asymmetry measurement is rather insensitive to systematic uncertainties such as acceptances and charge normalization. A significant contribution is expected from the beam polarization which is measured using Möller scattering with an accuracy of 0.010. Another contribution is due to possible contamination of the single photon sample with misidentified photons from π^0 events. As these events will have a different asymmetry from single photon events they add an systematic error to the asymmetry. With the additional photon detector we will have excellent separation of $p\gamma$ and $p(\pi^0 \to \gamma\gamma)$ events. The π^0 asymmetry will be measured simultaneously and can thus be corrected for, as the size of the π^0 contamination

Table 2: Indicative binning of data in Q^2 and x_B, together with the cross sections at the center of each bin and for $t = -.325$ GeV^2, $\phi = 90°$. The resulting number of counts are calculated according to Eq. 11, with $\Delta t = 0.15$ GeV^2 and $\Delta\phi = 30°$. See text for more explanations.

Q^2 (GeV^2)	x_B	σ (nb/GeV^4)	$\Delta Q^2 \cdot \Delta x_B$ (GeV^2)	$(\Delta\varphi_e)_{\rm eff}/2\pi$	N
$0.8 - 1.2$	$0.09 - 0.17$	0.45	0.03	0.34	38000
$0.8 - 1.2$	$0.17 - 0.27$	0.23	0.02	0.31	11000
$1.2 - 1.7$	$0.13 - 0.23$	0.18	0.04	0.40	23000
$1.2 - 1.7$	$0.23 - 0.35$	0.077	0.04	0.36	9000
$1.7 - 2.3$	$0.18 - 0.28$	0.10	0.05	0.46	18000
$1.7 - 2.3$	$0.28 - 0.42$	0.035	0.06	0.42	7200
$2.3 - 3.1$	$0.25 - 0.35$	0.056	0.05	0.54	12000
$2.3 - 3.1$	$0.35 - 0.50$	0.018	0.08	0.50	5800
$3.1 - 4.1$	$0.35 - 0.55$	0.015	0.12	0.64	9300

can be measured as well. From the analysis of the 4.25 GeV data we conclude that the $ep(\pi^0)$ yield is generally smaller than the $ep(\gamma)$ yield except for some extreme kinematics where it may be comparable or larger.

We conservatively estimate the total systematic error of the asymmetry to ≈ 0.03. Since the peak asymmetry is expected to be 0.35, this will result in a 3% relative systematic error, sufficiently small for a very significant measurement.

Note that for the analysis of $ep \rightarrow epX$ events from the E1-6 data, the systematic error should be about 2-3 times larger.

The secondary goal of the experiment will be a measurement of the absolute cross section differences for the DVCS process. CLAS was designed to measure absolute cross sections at the 3% level. Currently, accuracies of 2-5% have been achieved in the measurement of elastic ep cross sections. Another process that can be used for absolute normalization is $ep \rightarrow ep\pi^0$ at the peak of the $\Delta(1232)$ resonance. The cross section is known with an accuracy of better than 3%. Measurement of this reaction requires detection of the scattered electron and the outgoing proton. Measurements with CLAS show agreement with fits to the world data at the level of better than 5%. In addition to the epX cross section uncertainty we estimate a 3% uncertainty in the photon detection efficiency.

Adding all systematic errors in quadrature, we obtain an estimate of 6.5% total systematic uncertainty for the $ep \rightarrow ep\gamma$ cross section.

When extracting the helicity-dependent cross section difference, the uncertainty in the beam polarization measurement, which we estimate at $\delta P_e \approx 0.015$, has to be taken into account as well.

7.2 Projected results and comparison to models

The following three graphs show some expected variations of the observables and a selection of expected data points.

Figure 23 shows the t dependence of the cross section and of the beam spin asymmetry, for three bins in Q^2 and x_B. Expected data points are shown only for $Q^2 = 2$ GeV^2 and $x_B = 0.35$, assuming a finer binning in t (compared to the discussion in Sec. 7): $\Delta t = 0.06$ GeV^2.

Figure 24 illustrates the x_B dependence, for various other fixed parameters. In this case, a finer binning in x_B was assumed: $\Delta x_B = 0.04$.

Finally, Fig. 25 shows the ϕ dependence, and the expected data points are shown with the original binning of Sec. 7.

Comparison with different models for the ξ-dependency of GPDs are included, together with a first estimation of the twist-3 effects for this process.

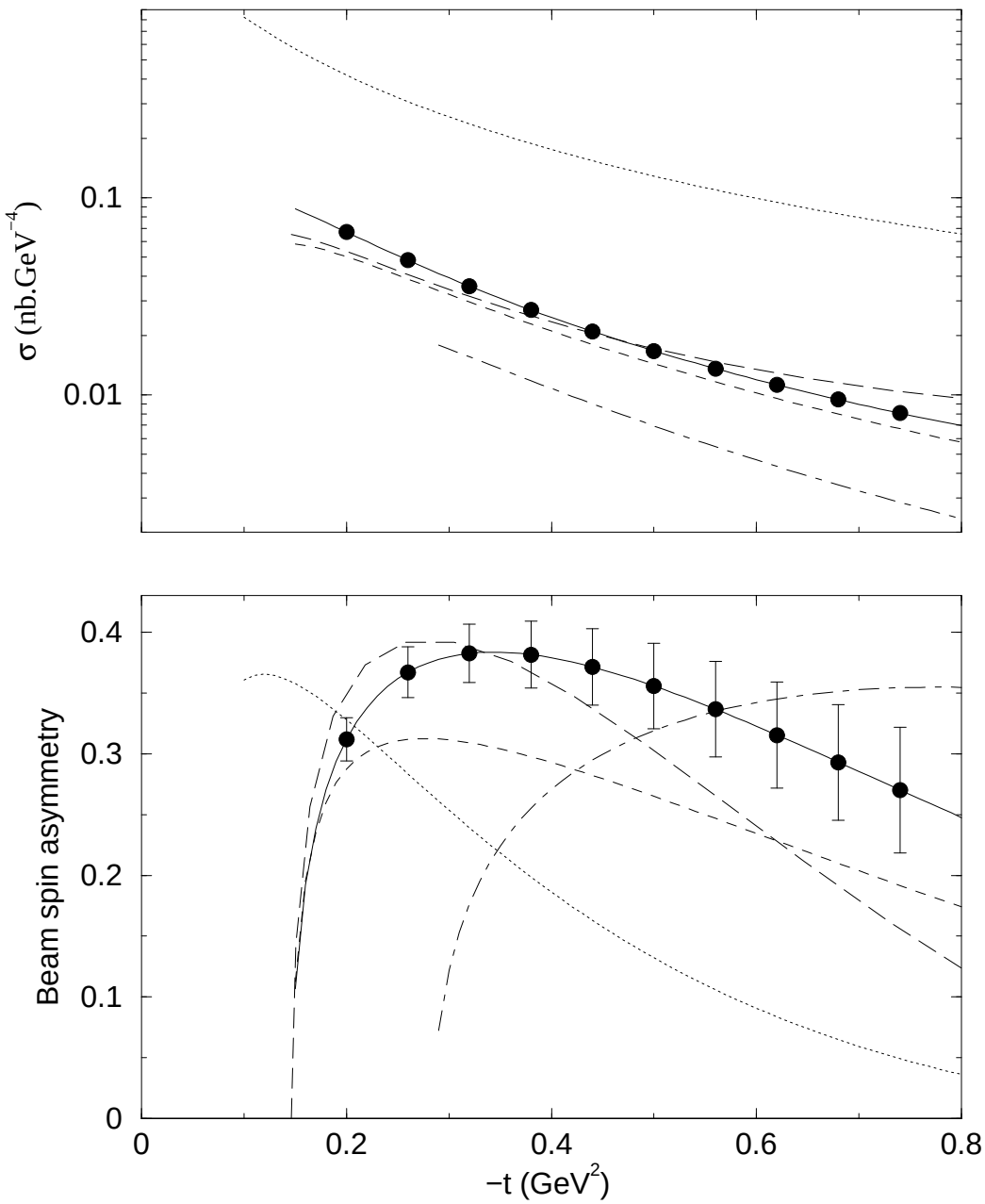

Figure 23: t-dependence of $ep \rightarrow ep\gamma$ observables at 6 GeV, for $\phi = 90°$ and $Q^2 = 1$ GeV^2, $x_B = .22$ (dotted curve), $Q^2 = 2$ GeV^2, $x_B = .35$ (solid), $Q^2 = 3.6$ GeV^2, $x_B = .45$ (dot-dashed), calculated with the ξ-dependent GPDs of Refs. [10, 22]. From the same references is also shown the ξ-independent version (dashed), and from Ref. [24] the calculation including twist-3 effects (long-dashed), both at $Q^2 = 2$ GeV^2. The points illustrate the expected statistical accuracy, for the bin sizes indicated in Sec. 7, except for $\Delta t = 0.06$ GeV^2.

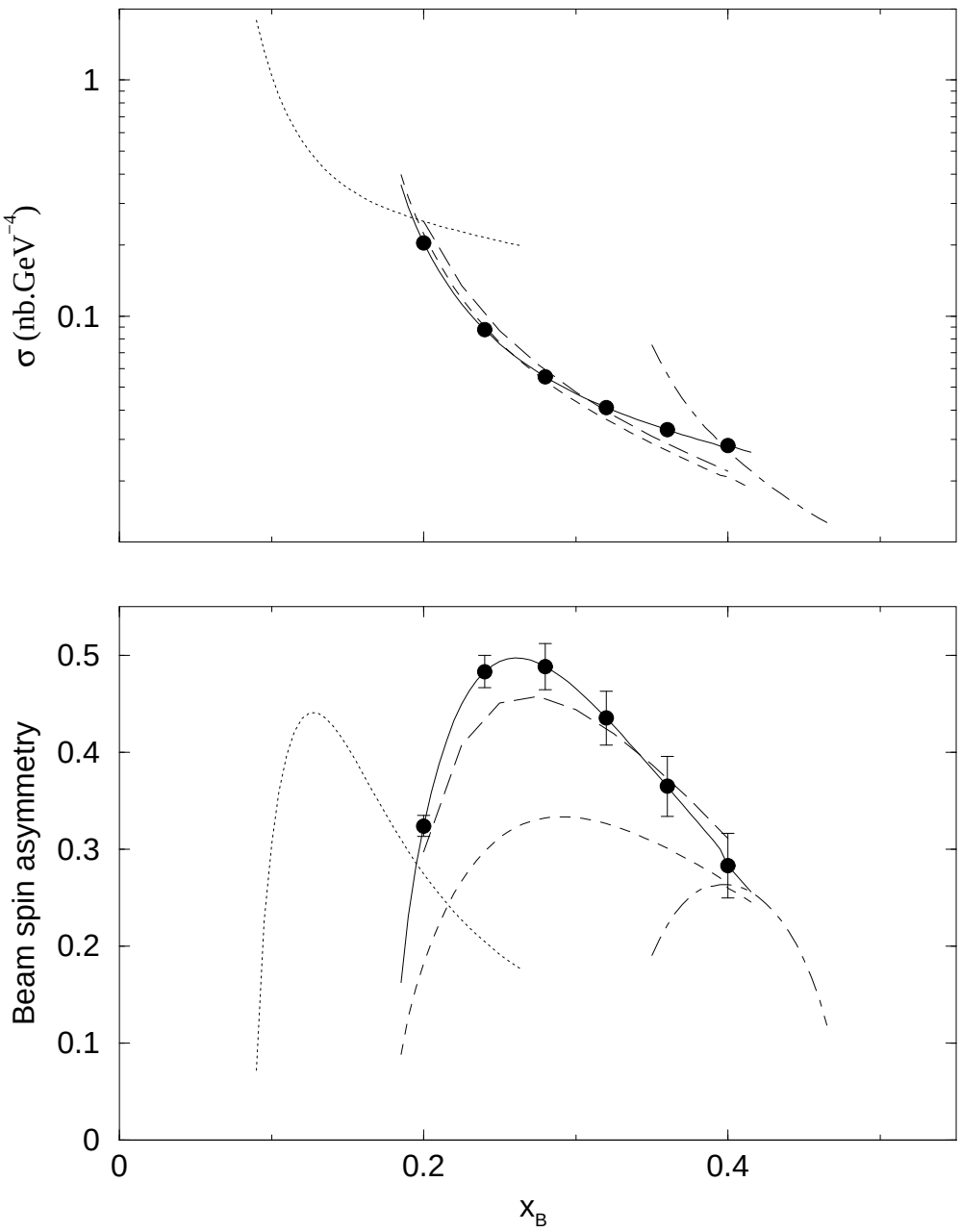

Figure 24: x_B-dependence of $ep \rightarrow ep\gamma$ observables at 6 GeV, for $\phi = 90°$, $t = -0.325$ GeV^2 and $Q^2 = 1$ GeV^2 (dotted curve), $Q^2 = 2$ GeV^2 (solid, dashed, long-dashed), $Q^2 = 3.6$ GeV^2 (dot-dashed). See Fig. 23 for remainder of the legend. The points illustrate the expected statistical accuracy, for the bin sizes indicated in Sec. 7, except for $\Delta x_B = 0.04$.

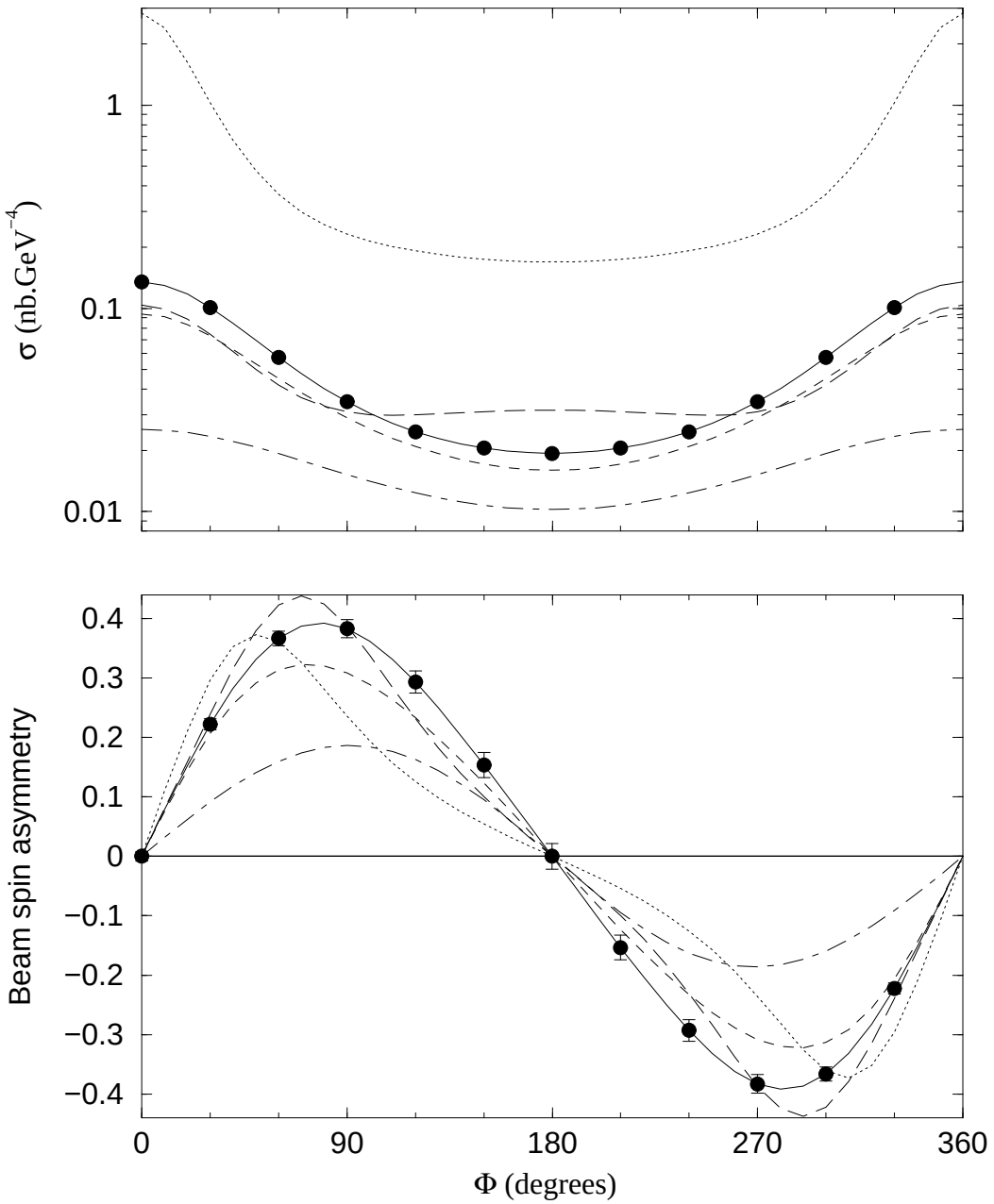

Figure 25: in Sec:4.3 ϕ-dependence of $ep \rightarrow ep\gamma$ observables at 6 GeV, for $t = -0.325$ GeV^2. The points illustrate the expected statistical accuracy at $Q^2 = 2$ GeV^2, for the bin sizes indicated in Sec. 7. See Fig. 23 for remainder of the legend.

8 Summary and beam time request

A dedicated DVCS experiment in Hall B, E01-113, approved by JLab PAC20, ran in part during spring 2005. The major part of the data taking was performed at the proposed luminosity of 2×10^{34} cm^{-2}sec^{-1}. 43% of the required data for the whole experiment was collected. Overall, the run was very successful. The DVCS collaboration built, commissioned and installed two new devices in CLAS, a superconducting solenoid magnet and a 424-channel $PbWO_4$ crystal calorimeter. Both devices were critical for this experiment and both showed excellent performance during the run. Currently the solenoid magnet is used in CLAS for the BoNuS experiment and few other experiments have already been approved or are proposed, that will use the calorimeter and/or the solenoid magnet together with CLAS.

Although a significant amount of data was collected, we are short of achieving the goals of the original proposal E01-113 in terms of mapping out Q^2, x_B and t dependences of the DVCS beam spin asymmetry. We thus request to run the remaining portion of the beam time at designed luminosity approved by PAC20. Taking into account the integrated luminosity during the first run, we now seek new approval (under jeopardy) for 34 days, necessary to achieve the goals of proposal E01-113.

We believe that the measurements of E01-113 and those that we intend to carry out in this proposal are a mandatory prerequisite for the development of the GPD field. This kind of study involves a simultaneous scan of various variables (x_B, Q^2, t), so that a large acceptance detector such as CLAS is most suitable.

The proposed DVCS measurement, together with the expected Hall A results, and the results of approved DVCS experiment with polarized proton target in CLAS will produce precision data on the imaginary part of the DVCS amplitude that will provide stringent tests of leading twist dominance and of models for GPDs, which will unlikely be superseded by any of the currently planned DVCS experiments. Precise data for the DVCS process at 6 GeV, produced in a timely fashion, will not suffer from the expected competition with HERMES, and will help maintain the momentum in the theory community. We finally want to point out that the study of DVCS and Deeply Virtual Meson Production has been proposed as a major program for the 12 GeV energy upgrade of CEBAF.

References

[1] X. Ji, Phys. Rev. Lett. **78**, 610 (1997); Phys. Rev. D **55**, 7114 (1997).

[2] A.V. Radyushkin, Phys. Lett. **B380**, 417 (1996); Phys. Rev. D **56**, 5524 (1997).

[3] S. Stepanyan *et al.* (CLAS collaboration), Phys. Rev. Lett. **87**, 182002 (2001).

[4] D. Müller *et al.*, Fortschr. Phys. **42** (1994) 2, 101.

[5] J.C. Collins, L. Frankfurt, and M. Strikman, Phys. Rev. D **56**, 2982 (1997).

[6] X. Ji, W. Melnitchouk and X. Song Phys. Rev. D **56**, 5511 (1997).

[7] V.Yu. Petrov et al., Phys. Rev. D **57**, 4325 (1998).

[8] M. Diehl, T. Feldmann, R. Jakob and P. Kroll, Eur. Phys. J. C **8**, 409 (1999).

[9] A.V. Radyushkin, Phys. Lett. **B449**, 81 (1999).

[10] M. Vanderhaeghen, P.A.M. Guichon and M. Guidal, Phys. Rev. **D60**, 094017 (1999).

[11] M. Burkardt, Int. J. Mod. Phys. **A18**, 173 (2003).

[12] J.P. Ralston and B. Pire, Phys. Rev. D **66**, 111501 (2002).

[13] B.W. Filippone and X. Ji, Adv. Nucl. Phys. **26**, 1 (2001).

[14] K. Goeke, M.V. Polyakov and M. Vanderhaeghen, Prog. Part. Nucl. Phys. **47**, 401 (2001).

[15] M. Diehl, Phys. Rep. **388**, 41 (2003).

[16] X. Ji, Ann. Rev. Nucl. Part. Sci **54**, 413 (2004).

[17] P. Kroll, Prog. Part. Nucl. Phys. **55**, 281 (2005).

[18] A.V. Belitsky and A.V. Radyushkin, Phys. Rep. **418**, 1 (2005).

[19] M. Garçon, Eur. Phys. J. A **18**, 389 (2003).

[20] J. Gronberg et al. (CLEO Collaboration), Phys. Rev. **D 57**, 33 (1998).

[21] I. V. Musatov and A. V. Radyushkin, Phys. Rev. D **56**, 2713 (1997).

[22] M. Vanderhaeghen, M. Guidal, P. Guichon, and L. Mossé, "Computer Codes for DVCS and BH Calculations", private communications.

[23] M. Diehl *et al.*, Phys. Lett. **B411**, 193 (1997).

[24] N. Kivel, M.V. Polyakov and M. Vanderhaeghen, Phys. Rev. D **63**, 114014 (2001); and M. Vanderhaeghen, private communication.

[25] F. Cano and J.-M. Laget, Phys. Lett. **B551**,317 (2003); erratum, ibid. **B571**,250 (2003).

[26] M. Guidal, M. Garçon, E. Smith *et al.*, CEBAF experiment E99-105.

[27] L. Morand *et al.* (CLAS Collaboration), Eur. Phys. J. A **24**, 445 (2005).

[28] C. Hadjidakis *et al.* (CLAS Collaboration), Phys. Lett. **B605**, 256 (2005).

[29] P. Bertin, C. Hyde-Wright, R. Ransome, F. Sabatié *et al.*, CEBAF experiment E00-110.

[30] P. Bertin, C. Hyde-Wright, F. Sabatié, E. Voutier *et al.*, CEBAF experiment E03-106.

[31] A. Biselli, L. Elouadhriri, K. Joo, S. Niccolai et al., CEBAF experiment E05-114.

[32] A. Airapetian *et al.* (HERMES Collaboration), Phys. Rev. Lett. **87**, 182001 (2001).

[33] C. Adloff *et al.* (H1 Collaboration), Phys. Lett. **B517**, 47 (2001).

[34] A. Aktas *et al.* (H1 Collaboration), Eur. Phys. J. **C44**, 1 (2005).

[35] S. Chekanov *et al.* (ZEUS Collaboration), Phys. Lett. **B573**, 46 (2003).

[36] N. d'Hose *et al.*, Eur. Phys. J. A **19** (2004) SUPPL147.

[37] Francesca Nessi-Tedaldi, CMS conference report, presented at Beauty'97, 5th International workshop on B-Physics at Hadron machines. Los Angeles (USA), 13-17 October 1997.

[38] R. Niyazov and S. Stepanyan, CLAS-Note 2005-021.

[39] F.-X. Girod, CLAS-Note 2005-023.

[40] F.-X. Girod and M. Garçon, CLAS-Note 2005-001.

[41] V. Kubarovsky, communication to the DVCS working group.